

A simple model for daily basin-wide thermodynamic sea ice thickness growth retrieval methodology: Stefan's Law Integrated Conducted Energy (SLICE)

James Anheuser¹, Yinghui Liu², and Jeffrey R. Key²

¹AOS UW-Madison, Madison, Wisconsin

²Center for Satellite Applications and Research, NOAA/NESDIS, Madison, Wisconsin

Correspondence: James Anheuser (anheuser@wisc.edu)

Abstract. As changes to Earth's polar climate accelerate, the need for robust, long-term sea ice thickness observation datasets for monitoring those changes and for verification of global climate models is clear. By ~~coupling linking~~ a recently developed algorithm for retrieving snow–ice interface temperature from passive microwave satellite data to a thermodynamic sea ice energy balance relation known as Stefan's Law, we have developed a new retrieval method for estimating thermodynamic sea ice thickness growth from space: Stefan's Law Integrated Conducted Energy (SLICE). ~~With an initial condition at the beginning of the sea ice growth season, the method can model basin-wide absolute sea ice thickness by combining the one-dimensional SLICE retrieval with an ice motion dataset.~~ The advantages of the SLICE retrieval method include daily basin-wide coverage and a potential for use beginning in 1987. ~~The method requires an initial condition at the beginning of the sea ice growth season in order to produce absolute sea ice thickness and cannot as yet capture dynamic sea ice thickness changes.~~ Validation of the method against ~~retrieval against measurements from~~ ten ice mass balance buoys ~~using the ice mass balance buoy thickness as the initial condition~~ show a mean correlation of ~~0.991~~ ~~0.88~~ and a mean bias of ~~0.008~~ ~~0.08~~ m over the course of an entire sea ice growth season. ~~Estimated Arctic basin-wide sea ice thickness from SLICE for the sea ice growth seasons beginning between 2012 through 2019 capture a mean of 12.0% less volumetric growth than a CryoSat-2 and Soil Moisture and Ocean Salinity (SMOS) merged sea ice thickness product (CS2SMOS) and a mean of 8.3% more volumetric growth than Despite its simplifications and assumptions relative to models like~~ the Pan-Arctic ~~Ice–Ocean~~ Modeling and Assimilation System (PIOMAS). ~~The spatial distribution of the sea ice thickness differences between the retrieval results and those reference datasets show patterns consistent with expected sea ice thickness changes due to dynamic effects. This new retrieval method is a viable basis for a long-term sea ice thickness climatology, especially if dynamic effects can be captured through inclusion of an ice motion dataset.~~

~~20 , basin-wide SLICE performs equally to PIOMAS when compared against CryoSat-2 and Operation IceBridge.~~

1 Introduction

Observing sea ice concentration and areal extent from satellites is a well established practice (Liu et al., 2016; Meier et al., 2017; Markus and Cavalieri, 2000; Markus and Cavalieri, 2009; Comiso, 2009; Lavergne et al., 2019). There are methods

based on data in the visual, infrared and microwave wavelength bands and climate data records produced from these methods
25 are commonly cited as polar climate indicators (Stroeve et al., 2012; Screen and Simmonds, 2010; Liu et al., 2009).

While sea ice concentration is more readily observed, sea ice thickness provides a more complete characterization of the state of the climate system because it allows for calculation of sea ice volume and latent heat release. Recent literature has made clear that reliable long-term observations of basin wide sea ice thickness are needed in order to constrain the representations of sea ice in global climate models (Mayer et al., 2019). Sea ice thickness based observations of sea ice volume can be used along
30 with other observations to refine the large range of projected sea ice area and volume across coupled global climate models (Docquier and Koenigk, 2021). Indeed, the lack of reliable long term sea ice thickness observation constraints is the primary barrier to reducing the uncertainty in future sea ice area and volume projections (Massonnet et al., 2018).

Sea ice thickness derived from space-based altimetry data collected by satellites like CryoSat-2 and IceSat-2-ICESat-2 stand as the current state of the art ~~but are limited in spatial coverage and temporal resolution~~ (Connor et al., 2009; Kwok and Cunningham, 2008; Markus et al., 2017; Wingham et al., 2006; Laxon et al., 2013). Though the instruments aboard these satellites have relatively high spatial resolutions, it takes 28 days and 91 days, respectively, for CryoSat-2 and ICESat-2 to cover the entire Arctic due to their relatively low spatial coverage (Wang et al., 2016). Other strategies for retrieving sea ice thickness include ~~the use of~~ a one-dimensional surface energy balance model driven by satellite products (Key et al., 2016) and ~~the use of low-frequency passive microwave satellite data for~~ estimating the thickness of thin sea ice (Meeklenburg et al., 2012).
40 ~~. Assimilating available observational data into a global coupled ocean-sea ice model is also effective using low-frequency passive microwave satellite data (Meeklenburg et al., 2012). A coupled ocean-sea ice model with assimilated observational data is also commonly referenced~~ (Zhang and Rothrock, 2003). A newer approach involves correlating sea ice thickness with sea ice age (Liu et al., 2020). The various available products are discussed and compared against one another both qualitatively and quantitatively in Wang et al. (2016) and against upward looking sonar (ULS) in Sallila et al. (2019).

Recent efforts to retrieve temperature at the boundary between snow and sea ice, referred to as the snow–ice interface temperature, have opened a new door in polar climate observation (Lee and Sohn, 2015; Lee et al., 2018; Kilic et al., 2019). These methods take advantage of radiances from the Advanced Microwave Scanning Radiometer (AMSR)-Earth Observing System (-E), AMSR2, the Special Sensor for Microwave Imager (SSM/I) and Special Sensor Microwave Imager/Sounder (SSMIS) passive microwave instruments using channels whose wavelengths are not significantly absorbed by snow and therefore carry
50 information from the snow–ice interface. Kang et al. (2021) demonstrated the utility of these snow–ice interface temperature data by using them to nudge a sea ice model, improving the model’s results. By coupling this newly available snow–ice interface temperature data with Stefan’s Law governing the thermodynamics of sea ice growth (Stefan, 1891; Lepparanta, 1993), we introduce a promising new method of estimating-retrieving thermodynamic sea ice thickness growth called Stefan’s Law Integrated Conducted Energy (SLICE).

As sea ice accretes on the underside of the ice layer, the latent heat of fusion conducts up through the ice to the snow–ice interface. In Stefan’s Law, that conducted heat and therefore rate of accretion is calculated using a heat conduction equation with the snow–ice interface temperature as the upper boundary condition and the local freezing temperature of sea water set as the lower boundary condition (Stefan, 1891; Lepparanta, 1993). By using the satellite retrieved snow–ice interface temperature

in this relationship and with an initial thickness condition in hand, SLICE is able to retrieve daily rate of ice accretion and model sea ice thickness on a basin-wide scale during the sea ice growth season. With the required passive microwave observations available from 1987 to current, there is potential for a by integrating these retrieved growth rates from an initial sea ice thickness time series of the same span condition. The methodology is applicable beginning in 1987 with the availability of the required passive microwave observations.

2 Data

The SLICE retrieval method described here utilizes passive microwave brightness temperatures and a passive microwave based sea ice concentration dataset. Modelling basin-wide sea ice thickness requires motion vectors and a satellite based initial condition. A preliminary validation of the retrieval method references sea ice thickness from ice mass balance buoy data, satellite radar altimeter data and a and airborne altimeter based sea ice thickness model reanalysis.

2.1 Snow-Ice Interface Temperature

Outgoing longwave radiation on the low frequency end of the microwave spectrum is not significantly absorbed by snow on the Earth's surface (Mathew et al., 2009). Previous efforts to take advantage of this fact to measure the temperature of sea ice have relied on infrared (IR) measurements or models to augment the results (Comiso, 1983; Hall et al., 2004; Hewison and English, 1999). This process leads to errors and IR data is only available in clear sky conditions. In Lee and Sohn (2015), only microwave brightness temperatures are used. The method uses the horizontal and vertical polarity 6.9 GHz channel brightness temperatures from the passive microwave AMSR-E or AMSR2 instruments along with a combined Fresnel relationship (Sohn and Lee, 2013) to determine the local microwave emissivity of sea ice. This emissivity along with the observed brightness temperatures yields the snow-ice interface temperature. We have replicated the procedure from Lee and Sohn (2015) for use in the retrieval method described here.

Assuming the absorption by snow and the atmosphere is negligible, the snow-ice interface temperature can be related to satellite observed brightness temperature from a channel with a weighting function peak at the snow ice interface through

$$T_{B,H}(\nu) = t_{atm}(\nu)\epsilon_H(\nu)T_{si}$$

$$T_{B,V}(\nu) = t_{atm}(\nu)\epsilon_V(\nu)T_{si}$$

where $T_{B,H}(\nu)$ is satellite observed horizontally polarized spectral brightness temperature, $\epsilon_H(\nu)$ is local snow-ice interface spectral emissivity for horizontal polarized emission and T_{si} is snow-ice interface temperature. This relationship also holds for vertically polarized satellite observed spectral brightness temperature and spectral emissivity $T_{B,V}(\nu)$ data, and $\epsilon_V(\nu)$. As such, the following relationship also holds:

$$\frac{\epsilon_H(\nu)}{\epsilon_V(\nu)} = \frac{1 - r_H(\nu)}{1 - r_V(\nu)} = \frac{T_H(\nu)}{T_V(\nu)}$$

where $r_H(\nu)$ and $r_V(\nu)$ are horizontal and vertical spectral reflectance, respectively. A combined Fresnel relationship closes

90 Equation ?? and allows solving for one of the emissivities (Sohn and Lee, 2013):

$$r_V(\nu) = \left(r_H(\nu)^2 \frac{1 + r_H(\nu)^{-1/2} \cos 2\theta}{1 + r_H(\nu)^{1/2} \cos 2\theta} \right)^2$$

where θ is satellite viewing angle. The resultant emissivity can be inserted into Equation ?? to solve for T_{si} . Additional detail can be found in Lee and Sohn (2015). sea ice models.

The AMSR-E and AMSR2 6.9 GHz channels were used to calculate snow–ice interface temperature here as in Lee and Sohn (2015) 95. The resultant snow–ice interface temperatures were found to require a bias correction of 5 K in order to match buoy snow–ice interface temperatures and in order to produce the best sea ice thickness retrieval method results. This bias correction may address atmospheric absorption and snow absorption to the extent that they cannot be assumed negligible. Figure 2 shows snow–ice interface temperatures on 1 January 2013 calculated from AMSR2 radiances.

2.1 Passive microwave brightness temperatures and sea ice concentration

100 Snow–ice interface temperatures on 1 January 2013 derived from AMSR2 radiances.

The AMSR-E and AMSR2 brightness temperatures available from the National Snow and Ice Data Center (NSIDC) were used in this study (https://nsidc.org/data/AE_SI25/versions/3; https://nsidc.org/data/AU_SI25/versions/1; Cavalieri et al., 2014; Markus et al., 2018). The AMSR-E data is available for June 2002 through October 2011 and the AMSR2 data is available for July 2012 to the present. The AMSR2 data has been intercalibrated with the AMSR-E data and the brightness temperatures 105 between these two instruments are treated here as a continuous dataset (Markus et al., 2018). The data is provided on a 25 km polar stereographic grid, but when needed on a basin-wide scale for use with the sea ice thickness retrieval method described here, the data were linearly interpolated to a 25 km Equal-Area Scalable Earth (EASE)-Grid 2.0 grid. In Lee et al. (2018), the method is adapted for use with the

The NASA Team 2 algorithm is a passive microwave brightness temperature sea ice concentration algorithm (Markus and Cavalieri, 2000) 110. It is an enhancement to the original NASA Team algorithm (Cavalieri et al., 1984; Gloersen and Cavalieri, 1986) in that it adds 85 GHz frequency brightness temperatures to the original algorithm, which used only 19 GHz and 37 GHz data, in order to better account for interference from surface effects. The algorithm utilizes open ocean and 100% ice concentration tie points in polarization and spectral gradient ratios to determine sea ice concentration. While originally developed for use with SSM/I 115 49.35 GHz channel to allow for retrieval of data (Markus and Cavalieri, 2000), the algorithm was planned to be and is now in use with AMSR-E and AMSR2 data. Here we use this AMSR-E and AMSR2 sea ice concentration data, which is available from the NSIDC as a part of the same dataset that contains the brightness temperatures used to calculate snow–ice interface temperature beginning in 1987. (Cavalieri et al., 2014; Markus et al., 2018).

Liquid water at the emitting layer in the form of open ocean or melt ponds interferes with the snow–ice interface temperature algorithm (Lee and Sohn, 2015). As such and in line with Lee and Sohn (2015), the snow–ice interface is only calculated here 120 in grid cells with greater than 95% sea ice concentration. A method for calculating snow–ice interface temperature for grid

cells with under 95% sea ice concentration is described in the appendix of Lee and Sohn (2015) but is not implemented here pending further investigation. The snow–ice interface temperature retrieval is also subject to the polar data gap associated with

2.2 Sea ice motion vectors

125 Sea ice is not static, but rather a dynamic collection of variably sized parcels that are each in constant horizontal motion under the effects of wind, ocean currents and internal stress. In order to treat sea ice in a lagrangian sense, the motion of these parcels must be understood. Here we use the Polar Pathfinder Daily 25 km EASE-Grid Sea Ice Motion Vectors, Version 4 available from the NSIDC (Tschudi et al., 2019; Tschudi et al., 2020). The product is available from 1978 to present at daily and weekly temporal resolution, each with basin-wide coverage and each on the 25 km EASE-Grid. Using an optimal
130 interpolation scheme, ice motion vectors are created from cross correlated satellite brightness temperature data from AMSR-E, Advanced Very High Resolution Radiometer (AVHRR), Scanning Multichannel Microwave Radiometer (SMMR), SSM/2 data. For basin-wide analysis, I and SSMIS, along with International Arctic Buoy Program (IABP) buoy locations and a National Centers for Environmental Protection (NCEP)/ National Center for Atmospheric Research (NCAR) wind reanalysis data derived free drift estimate. Each satellite and buoy dataset are included in the polar data gap is filled using two-dimensional
135 linear interpolation, optimal estimation scheme only when available within the life span of the ice motion product. This means input data sources vary throughout the record. DeRepentigny et al. (2016) found the weekly sea ice motion vectors to have a 7% median error when compared against IABP buoys between 1988 and 2011.

2.3 Airborne and satellite based sea ice thickness products

CryoSat-2 carries the SAR/Interferometric Radar Altimeter-2 (SIRAL-2) instrument (Wingham et al., 2006; Laxon et al., 2013
140) and was launched by the European Space Agency (ESA) in 2010. Similar to other satellite altimeters, ice thickness is determined from CryoSat-2 data by first calculating the thickness of the sea ice above sea level—known as the freeboard—by determining the distance traveled by the radar signal between the satellite and the the ice surface and subtracting that distance from the satellite orbit altitude above sea level. An assumed snow loading provides a correction for the reduced propagation speed of the radar signal through snow. Then, the assumed snow loading and a hydrostatic balance is used to determine
145 sea ice mass which in turn is converted to thickness using an assumed density (Laxon et al., 2013). Gridded ice thickness products derived from ESA CryoSat-2 Level 1b data are provided by the Centre for Polar Observation and Modelling (CPOM) (Tilling et al., 2018), the National Aeronautics and Space Agency (NASA) Goddard Space Flight Center (GSFC) (Kurtz et al., 2014a), the Alfred Wegener Institute (Ricker et al., 2014; Hendricks and Ricker, 2020; Ricker et al., 2017a), the NASA Jet Propulsion Laboratory (Kwok and Cunningham, 2015), the ESA Climate Change Initiative (Hendricks et al., 2018) and the Laboratoire
150 d'Études en Géophysique et Océanographie Spatiales Center for Topographic studies of the Ocean and Hydrosphere (Guerreiro et al., 2017). The primary differences between these datasets relate to averaging period, grid sizing and radar response waveform retracking procedure.

155 The ESA Soil Moisture and Ocean Salinity (SMOS) satellite carries the Microwave Imaging Radiometer using Aperture
Synthesis (MIRAS) instrument which measures 1.4 GHz passive microwave brightness temperatures at 35 to 50+ km resolution
160 (Mecklenburg et al., 2012). While originally intended for measuring soil moisture and ocean salinity, the high penetration depth
of the 1.4 GHz channel into sea ice allows for retrieval of an ice temperature that when incorporated into a radiative transfer
model yields a sea ice thickness estimate (Tian-Kunze et al., 2014). This approach has associated uncertainties in sea ice below
0.5 m thick that are lower than those of satellite altimeters.
165 Sea ice thickness observations from SMOS and CryoSat-2 have complementing uncertainties. SMOS has high uncertainties
when measuring thick ice and CryoSat-2 has high uncertainties when measuring thin ice (Ricker et al., 2017b). This creates an
opportunity for synergy between the instruments. The AWI CS2SMOS dataset takes advantage of this synergy. By combining
the datasets through a weighted averaging scheme, root mean squared errors are reduced from 76 cm with CryoSat-2 alone to
66 cm and the squared correlation coefficient is increased from 0.47 with CryoSat-2 to 0.61 when compared against NASA
Operation Ice Bridge data (Ricker et al., 2017b). The AWI CS2SMOS dataset is available at a weekly time resolution and on a
25 km EASE-Grid 2.0 and was used with the method demonstrated here due to the high spatial coverage.

170 The NASA Operation IceBridge (OIB) mission is an airborne campaign comprising a series of flights covering the years
2009-2016, bridging the gap between the NASA Ice, Cloud and land Elevation Satellite (ICESat) and NASA ICESat-2 laser
altimeter satellite missions (Kurtz et al., 2013). Among the instruments aboard each OIB flight, of primary importance to
this study are the Airborne Topographic Mapper (ATM) instrument (Krabill et al., 1995) and snow radar (Panzer et al., 2013)
175 . The ATM is a laser altimeter whose return signal is used along with an aerial photography based sea ice lead (fracture)
discrimination algorithm to retrieve sea ice freeboard height at 40 m spatial resolution. The snow radar return signal is used to
determine snow depth. Sea ice freeboard and snow depth are used in conjunction with a hydrostatic balance to determine sea ice
thickness at the sea ice freeboard resolution of 40 m. We use OIB sea ice thickness from the IceBridge L4 Sea Ice Freeboard,
Snow Depth, and Thickness, Version 1 and its QuickLooks counterpart as provided by the NSIDC (Kurtz et al., 2015). Figure
1 shows OIB flight paths used in this study.

2.4 Ice Mass Balance Buoys

180 In order to statistically characterize the sea ice thickness retrieval method described herein, ice mass balance buoy data served
as the reference. The ice mass balance buoys were deployed and maintained by the United States Army Corps of Engineers
Cold Regions Research and Engineering Laboratory (CRREL) (Perovich et al., 2021). Undeformed ice floes are chosen for
buoy sites to ensure the buoy is representative of the surrounding ice (Polashenski et al., 2011).

~~Of particular relevance to comparison with the retrieval method described here, a buoy is a Lagrangian observation as it
travels with the ice pack rather than remaining geospatially stationary. The retrieval method calculates ice thickness change
and requires Lagrangian tracking of ice thickness making buoy data a good match for validation.~~

185 Data fields used from the buoys were sea ice thickness and geolocation in latitude and longitude. Ice thickness is observed
using two acoustic rangefinder sounders, one positioned above and one positioned below the ice. Each sounder has an accuracy
of 0.005 m (Richter-Menge et al., 2006). An Argos antenna mounted on the buoy transmits the geolocation and other observa-

tions at minimum twice per day (Richter-Menge et al., 2006). For this study, all data fields were resampled to 1 d resolution by calculating daily mean values. All buoys from the years 2003 to 2016 showing an entire season of sea ice thickness growth were used for comparison with the exception of buoys installed in landfast ice and those that show obvious dynamic ice deformation effects. Table 1 provides relevant details pertaining to the buoys used. Buoy 2013F spanned two winter seasons and as such has been divided into two buoy numbers, 2013F and 2013Fb, with 2013Fb covering the second winter season during which the buoy was deployed. As such, a deployment date is not listed for 2013Fb. Drift tracks from 1 November to 1 April for the buoys are shown in Fig. 1. The buoys are concentrated in the Central Arctic and Beaufort Sea.

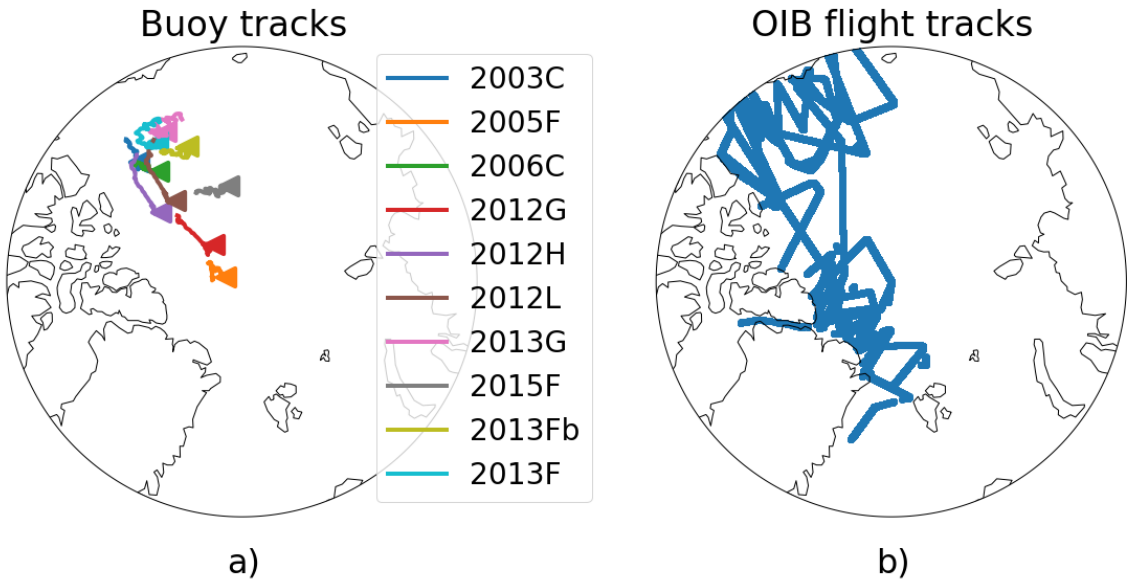


Figure 1. Tracks traveled by a) ice mass balance buoys and b) Operation IceBridge flights used in this study. Initial buoy location is signified with a left facing triangle and all buoy tracks from 1 November to 1 April.

Efforts to compare satellite based records of sea ice thickness with ground truth are hampered by the scale of the question. 195 Ground truth measurements of sea ice are necessarily taken from a single point while satellites observe sea ice thickness on the scale of kilometers. The variability of sea ice across those kilometers leads to uncertainty in the comparison. It has been shown, however, that while variability in absolute ice thickness may be significant on the scale of a satellite observation, sea ice growth and melt ~~is-are~~ relatively uniform on the satellite length scale (Polashenski et al., 2011). Therefore, while absolute comparisons of sea ice thickness between a ground truth and satellite observation may be tenuous, comparisons of growth over 200 a winter season between single point ground truth and satellite based observations are more robust.

~~CryoSat-2 is a currently operational radar altimeter (Wingham et al., 2006; Laxon et al., 2013) launched by the European Space Agency (ESA) in 2010. Similar to other satellite altimeters, ice thickness is determined from CryoSat-2 data by first calculating the thickness of the sea ice above sea level—known as the freeboard—and then assuming a snow loading and~~

Table 1. A listing of United States Army Corps of Engineers Cold Regions Research and Engineering Laboratory (CRREL) Ice Mass Balance buoys used in this work. All buoys from 2003 to 2016 containing a full season of sea ice thickness growth are included, excluding those in landfast ice or showing obvious dynamic effects.

Buoy	Region	Ice Type	Deployment date
2003C	Beaufort Sea	Multi-year	2002/8/31
2005F	Central Arctic	Multi-year	2005/9/3
2006C	Beaufort Sea	Multi-year	2006/9/4
2012G	Central Arctic	First year	2012/10/1
2012H	Beaufort Sea	First year	2012/9/10
2012L	Beaufort Sea	Multi-year	2012/8/27
2013F	Beaufort Sea	Multi-year	2013/8/25
2013G	Beaufort Sea	Multi-year	2013/9/4
2013Fb	Beaufort Sea	Multi-year	-
2015F	Central Arctic	Multi-year	2015/8/13

hydrostatic balance to determine sea ice mass which in turn is converted to thickness using an assumed density (Laxon et al., 2013). Gridded ice thickness products derived from ESA CryoSat-2 Level 1b data are provided by the ESA Centre for Polar Observation and Modelling (CPOM) (Tilling et al., 2018), the National Aeronautics and Space Agency (NASA) Goddard Space Flight Center (GSFC) (Kurtz et al., 2014a), the Alfred Wegener Institute (Ricker et al., 2014; Hendricks and Ricker, 2020; Ricker et al., 2017a), the NASA Jet Propulsion Laboratory (Kwok and Cunningham, 2015), the ESA Climate Change Initiative (Hendricks et al., 2018) and the Laboratoire d'Études en Géophysique et Océanographie Spatiales Center for Topographic studies of the Ocean and Hydrosphere (Guerreiro et al., 2017). The primary differences between these datasets relate to averaging period, grid sizing and radar response waveform retracking.

The ESA Soil Moisture and Ocean Salinity (SMOS) satellite carries the Microwave Imaging Radiometer using Aperture Synthesis (MIRAS) instrument which measures 1.4 GHz passive microwave brightness temperatures at 35 to 50+ km resolution (Meeklenburg et al., 2012). While originally intended for measuring soil moisture and ocean salinity, the high penetration depth of the 1.4 GHz channel into sea ice allows for retrieval of an ice temperature that when incorporated into a radiative transfer model yields a sea ice thickness estimate (Tian-Kunze et al., 2014). This approach has associated uncertainties in sea ice below 0.5 m thick that are lower than those of satellite altimeters.

Sea ice thickness observations from SMOS and CryoSat-2 have complimenting uncertainties. SMOS has high uncertainties when measuring thick ice and CryoSat-2 has high uncertainties when measuring thin ice (Ricker et al., 2017b). This creates an opportunity for synergy between the instruments. The AWI CS2SMOS dataset takes advantage of this synergy. By combining the datasets through a weighted averaging scheme, root mean squared errors are reduced from 76 cm with CryoSat-2 alone to 66 cm and the squared correlation coefficient is increased from 0.47 with CryoSat-2 to 0.61 when compared against NASA

225 Operation Ice Bridge data (Ricker et al., 2017b). The AWI CS2SMOS dataset is available at a weekly time resolution and on a 25 km EASE-Grid 2.0 and was used with the method demonstrated here due to the high spatial coverage.

225 2.5 PIOMAS

The Sea ice models AWI CS2SMOS

230 CryoSat-2 is a currently operational radar altimeter (Wingham et al., 2006; Laxon et al., 2013) launched by the European Space Agency (ESA) in 2010. Similar to other satellite altimeters, ice thickness is determined from CryoSat-2 data by first calculating the thickness of the sea ice above sea level—known as the freeboard—and then assuming a snow loading and hydrostatic balance to determine sea ice mass which in turn is converted to thickness using an assumed density (Laxon et al., 235 2013). Gridded ice thickness products derived from ESA CryoSat-2 Level 1b data are provided by the ESA Centre for Polar Observation and Modelling (CPOM) (Tilling et al., 2018), the National Aeronautics and Space Agency (NASA) Goddard Space Flight Center (GSFC) (Kurtz et al., 2014a), the Alfred Wegener Institute (Ricker et al., 2014; Hendricks and Ricker, 2020; Ricker et al., 2017a), the NASA Jet Propulsion Laboratory (Kwok and Cunningham, 2015), the ESA Climate Change Initiative (Hendricks et al., 2018) and the Laboratoire d'Études en Géophysique et Océanographie Spatiales Center for Topographic studies of the Ocean and Hydrosphere (Guerreiro et al., 2017). The primary differences between these datasets relate to averaging period, grid sizing and radar response waveform retracking.

240 The ESA Soil Moisture and Ocean Salinity (SMOS) satellite carries the Microwave Imaging Radiometer using Aperture Synthesis (MIRAS) instrument which measures 1.4 GHz passive microwave brightness temperatures at 35 to 50+ km resolution (Meeklenburg et al., 2012). While originally intended for measuring soil moisture and ocean salinity, the high penetration depth of the 1.4 GHz channel into sea ice allows for retrieval of an ice temperature that when incorporated into a radiative transfer model yields a sea ice thickness estimate (Tian-Kunze et al., 2014). This approach has associated uncertainties in sea ice below 0.5 m thick that are lower than those of satellite altimeters.

245 Sea ice thickness observations from SMOS and CryoSat-2 have complimentary uncertainties. SMOS has high uncertainties when measuring thick ice and CryoSat-2 has high uncertainties when measuring thin ice (Ricker et al., 2017b). This creates an opportunity for synergy between the instruments. The AWI CS2SMOS dataset takes advantage of this synergy. By combining the datasets through a weighted averaging scheme, root mean squared errors are reduced from 76 cm with CryoSat-2 alone to 66 cm and the squared correlation coefficient is increased from 0.47 with CryoSat-2 to 0.61 when compared against NASA Operation Ice Bridge data (Ricker et al., 2017b). The AWI CS2SMOS dataset is available at a weekly time resolution and on a 25 km EASE-Grid 2.0 and was used with the method demonstrated here due to the high spatial coverage.

2.5 PIOMAS

250 The Sea ice models The Pan-Arctic Ice–Ocean Modeling and Assimilation System (PIOMAS) is a numerical model reanalysis product that couples the Parallel Ocean Program (POP) model developed at Los Alamos National Laboratory with a thickness and enthalpy distribution (TED) model (Zhang and Rothrock, 2003). The TED model includes a viscous–plastic sea ice rheology (Hibler, 1979) and a sea ice thickness distribution scheme that accounts for redistribution due to ridging (Thorndike et al.,

1975). The model ~~is~~utilizes a generalized orthogonal curvilinear coordinate (GOCC) grid. The northern grid pole is shifted to be over Greenland where there is no ocean or sea ice, avoiding the need to deal with converging meridians and grid cell areas that approach zero. This shift also allows the highest grid resolutions to occur in the Canadian Archipelago, Baffin Bay and the Greenland Sea where the geography is intricate. The model ~~is~~ driven by daily surface forcing and sea surface temperatures (SSTs) provided by National Centers for Environmental Protection (NCEP) ~~NCEP/National Center for Atmospheric Research (NCAR)~~ NCAR and NSIDC sea ice concentration in order to produce daily sea ice thickness ~~data~~ distributions from 1978 to present (Schweiger et al., 2011). Here we use the daily effective sea ice thickness output which converts sea ice thickness distribution into a single effective thickness value for each grid cell.

2.5 AMSR-SIC

The NASA Team 2 algorithm is a passive microwave brightness temperature based sea ice concentration algorithm (Markus and Cavalieri, 2000). It is an enhancement to the original NASA Team algorithm (Cavalieri et al., 1984; Gloersen and Cavalieri, 1986) in that it adds 85 GHz frequency brightness temperatures to the original algorithm, which used only 19 GHz and 37 GHz data, in order to better account for interference from surface effects. The algorithm utilizes open ocean and 100% ice concentration tie points in polarization ratio and spectral gradient ratios to determine sea ice concentration. While originally developed for use with SSM/I data (Markus and Cavalieri, 2000), Additionally, the algorithm was planned to be and is now in use with AMSR-E and AMSR2 data. Here we use this AMSR-E and AMSR2 sea ice concentration data which is available from the NSIDC as a part of the same dataset that contains the brightness temperatures used to calculate ~~data~~ output from the sea ice model described in Kang et al. (2021), henceforth K21, was used to provide additional context. As briefly described in Sect. 1, K21 nudged a one-dimensional sea ice thermodynamic model with satellite retrieved snow–ice interface temperatures. The model itself is based on Maykut and Untersteiner (1971) and is a multi-layer numerical approximation for the snow and sea ice system. While the model is driven by European Centre for Medium-Range Weather Forecasts (ECMWF) ERA-Interim reanalysis data, temperatures at the snow–ice interface are nudged using the same snow–ice interface temperature retrieval used here (Lee and Sohn, 2015) in a non-physical correction term. This method was extrapolated to basin-wide results through the use of lagrangian tracking of individual sea ice parcels. The SLICE model is similar but greatly simplified and driven directly by the snow–ice interface temperature (https://nsidc.org/data/AE_SI25/versions/3; https://nsidc.org/data/AU_SI25/versions/1; Cavalieri et al., 2014; Markus et al., 2018). ~~retrieval~~

3 Methodology

Sea ice grows thicker through two primary physical mechanisms: thermodynamic phase change and dynamic changes due to the relative motion of the ice pack. The governing equation for a ~~Eulerian~~ sea ice thickness ~~field~~ can be written as

$$\frac{\partial H}{\partial t} = f(t, H, \mathbf{x}) - \nabla \cdot (\mathbf{u}H), \quad (1)$$

where H is plane slab sea ice thickness, t is time, f is a function of time, thickness and position vector \mathbf{x} describing thermodynamic sea ice thickness increase, and \mathbf{u} is the ice motion vector. This equation is analogous to [Equation Eq. \(3\)](#) in (Thorndike et al., 1975), but does not include the redistribution term [in that equation](#) because here we use a plane slab thickness H rather than a thickness distribution. The second term on the right hand side of [Equation Eq. \(1\)](#) captures dynamic thickness changes.

290 [The focus in the remainder of this section will be on](#), including both advection and deformation of sea ice. Through the following methodology called Stefan's Law Integrated Conducted Energy (SLICE), we retrieve the first term on the right hand side of [Equation Eq. \(1\)](#) and use a parcel tracking approach to approximate sea ice advection and model basin-wide thickness.

[By coupling the conductive heat equation to a latent heat of freezing term, Stefan's Law relates the rate of thermodynamic sea ice thickness increase to the temperature difference between the](#)

295 **3.1 Snow–Ice Interface Temperature**

Outgoing longwave radiation on the low frequency end of the microwave spectrum is not significantly absorbed by snow on the Earth's surface (Mathew et al., 2009). Previous efforts to take advantage of this fact to measure the temperature of sea ice have relied on infrared (IR) measurements or models to augment the results (Comiso, 1983; Hall et al., 2004; Hewison and English, 1999). This process leads to errors and IR data is only available in clear sky conditions. In Lee and Sohn (2015), only 300 microwave brightness temperatures are used. The method uses the horizontally and vertically polarized 6.9 GHz channel brightness temperatures from the passive microwave AMSR-E or AMSR2 instruments along with a combined Fresnel relationship (Sohn and Lee, 2013) to determine the local microwave emissivity of sea ice. This emissivity along with the observed brightness temperatures yields the snow–ice interface temperature. In Lee et al. (2018), the method is adapted for use with the SSM/I 19.35 GHz channel to allow for retrieval of snow–ice interface temperature beginning in 1987. We have adapted the procedure from 305 Lee and Sohn (2015) for use in the retrieval method described below.

3.1.1 Atmospheric Transmittance

In order to accurately retrieve snow–ice interface temperature using passive microwave brightness temperatures, the effect of the atmosphere on these satellite observed brightness temperatures must be understood and accounted for. Atmospheric transmittance at 6.9 GHz was estimated using the Radiative Transfer for TOVS v12 (RTTOV v12; Saunders et al., 2018) 310 radiative transfer model driven by ECMWF ERA5 reanalysis data (Hersbach et al., 2020, 2018).

The RTTOV model is capable of simulating brightness temperatures and other radiative characteristics of the Earth system as observed by roughly 90 space-borne sensors, including AMSR-E and [bottom of the ice layer, the later of which is at or very near to the freezing temperature of sea ice \(Stefan, 1891; Lepparanta, 1993\)](#). The physical explanation for this relationship is that the latent heat of freezing at the bottom of the ice is conducted up to AMSR2. For this study, the RTTOV direct radiative transfer model Python wrapper was used to simulate atmospheric transmittance for the AMSR-E and AMSR2 6.9 GHz channels, of 315 which both vertical and horizontal polarizations yield the same results. The AMSRE and AMSR-2 satellite zenith viewing angle of 55° was accounted for along with a sea ice surface type. Temperature and humidity profiles at 37 pressure levels along with skin temperature, surface pressure, 2 m temperature, 2 m humidity and 10 m winds were provided by ERA5 reanalysis

320 data at monthly temporal resolution and 1° spatial resolution from 2003 through 2020. The result is a dataset of monthly, 1° atmospheric transmittance for the snow–ice interface. 6.9 GHz AMSR-E and AMSR2 channels from 2003 to 2020 at monthly temporal and 1° spatial resolutions. These transmittance values were used in the calculation of snow–ice interface temperature.

3.1.2 Combined Fresnel Equation

325 Assuming absorption by snow is negligible, the snow–ice interface temperature can be related to satellite observed brightness temperature from a channel with a weighting function peak at the snow ice interface through the following two relationships:

$$T_{B,H}(\nu) = t_{atm}(\nu)\epsilon_H(\nu)T_{si} \quad (2)$$

$$T_{B,V}(\nu) = t_{atm}(\nu)\epsilon_V(\nu)T_{si}, \quad (3)$$

330 where $T_{B,H}(\nu)$ and $T_{B,V}(\nu)$ are satellite observed horizontally and vertically polarized spectral brightness temperatures, respectively, $t_{atm}(\nu)$ is spectral atmospheric transmittance, $\epsilon_H(\nu)$ and $\epsilon_V(\nu)$ are local snow–ice interface spectral emissivity for horizontal polarized and vertical polarized emission, respectively, and T_{si} is snow–ice interface temperature.

Eqs. (2) and (3) form a system of two equations with three unknowns— $\epsilon_H(\nu)$, $\epsilon_V(\nu)$ and T_{si} . Assuming reflectivity and emissivity sum to unity in both polarizations, a combined Fresnel relationship closes this system and allows solving for T_{si} :

$$r_V(\nu) = \left(r_H(\nu)^2 \frac{1 + r_H(\nu)^{-1/2} \cos 2\theta}{1 + r_H(\nu)^{1/2} \cos 2\theta} \right)^2, \quad (4)$$

335 where θ is satellite viewing angle, and $r_H(\nu)$, $r_V(\nu)$ are horizontal and vertical polarized spectral reflectance, respectively. Additional detail can be found in Lee and Sohn (2015).

Liquid water at the emitting layer in the form of open ocean or melt ponds interferes with the snow–ice interface temperature algorithm (Lee and Sohn, 2015). As such, and in line with Lee and Sohn (2015), the snow–ice interface is only calculated here in grid cells with greater than 95% sea ice concentration. A method for calculating snow–ice interface temperature for grid cells with under 95% sea ice concentration is described in the appendix of Lee and Sohn (2015) but is not implemented here pending further investigation.

3.2 Thermodynamic sea ice thickness growth

345 A simple model of one-dimensional thermodynamic sea ice thickness growth is a balance of heat fluxes where phase change is occurring, i.e., at the interface between the solid sea ice and liquid sea. These heat fluxes are latent heat released during the phase change of liquid sea water to solid sea ice, F_l , basal heat flux from the liquid sea to the solid ice, F_w , and heat conducted through the ice and away from the phase change interface, F_c . These three fluxes are balanced at the phase change interface as follows:

$$F_l + F_w = F_c. \quad (5)$$

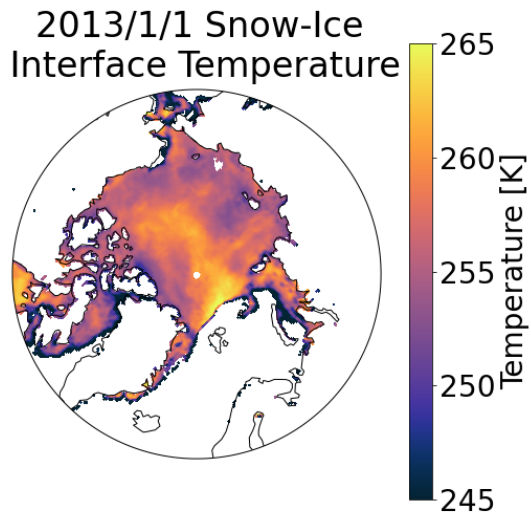


Figure 2. Snow–ice interface temperatures on 1 January 2013 derived from AMSR2 radiances.

When the snow–ice interface temperature drops below the temperature at the bottom of the ice, heat provided by basal flux and the latent heat of freezing is pulled to the snow–ice interface. In the method described here, a new–satellite observation 350 of snow–ice interface temperature (Lee and Sohn, 2015) drives the analytical solution to the this energy balance in order to determine sea ice thickness growth.

3.2.1 Stefan’s Law

By balancing the conductive heat equation with a latent heat of freezing and basal heat flux term, Stefan’s Law relationship in order to determine relates the rate of thermodynamic sea ice thickness growth increase to the temperature difference between 355 the snow–ice interface and bottom of the ice layer, the later of which is at or very near to the freezing temperature of sea ice (Stefan, 1891; Lepparanta, 1993).

Just as fluid flows across a pressure difference and electricity flows across a voltage difference, all heat transfer occurs across a temperature difference. Conduction is the transfer of heat across a solid medium and is always accompanied by a temperature difference across that medium. The equation governing one-dimensionalone-dimensional, steady state conduction is through 360 sea ice is

$$F_c = \frac{-\kappa}{H} \frac{\kappa_{eff}}{H} \left(T_{2f} - T_{1si} \right) / D, \quad (6)$$

where \dot{q} is heat per unit area or heat flux, κ is κ_{eff} is the thermal conductivity of the medium, T_1 and T_2 are the boundary temperatures and D is the distance between the boundaries sea ice, H is sea ice thickness, T_f is the freezing point of sea water and T_{si} is the snow-ice interface temperature.

365 A change in the phase of a material must either release or accept energy as the molecular bonds and motion within the material change. In the case of a phase change from liquid to solid, energy is released as the molecular motion is reduced with the introduction of molecular bonds. The equation describing the one-dimensional latent heat release in this scenario is as sea water changes phase from liquid to solid is:

$$F_l = \rho_{si} L \frac{dD}{dt} \frac{dH}{dt}, \quad (7)$$

370 where \dot{q} is heat per unit area or heat flux, ρ_s is ρ_i is the density of the solid phase of the material, L is the latent heat of fusion and $\frac{dD}{dt}$ is the one-dimensional change in solid material size $\frac{\partial H}{\partial t}$ is the change in sea ice thickness per unit time.

In Stefan's Law, Equations 6 and 7 are combined via the common heat flux term, \dot{q} to form Eqs. (6) and (7) are substituted into Eq. (5) to form

$$\rho_i L \frac{\partial H}{\partial t} = \frac{\kappa_i}{\rho_i L H} \frac{\kappa_{eff}}{H} (T_f - T_{si}) - F_w. \quad (8)$$

375 where ρ_i is the density of sea ice, L is the latent heat of fusion of sea ice, $\frac{\partial H}{\partial t}$ is the change in sea ice thickness per unit time, κ_i is the thermal conductivity of sea ice, T_f is the freezing point of sea water, T_{si} is the snow-ice interface temperature and H is sea ice thickness (Lepparanta, 1993). There are a number of assumptions inherent Isolating for sea ice thermodynamic growth rate, we have

$$\frac{\partial H}{\partial t} = \frac{\kappa_{eff}}{\rho_i L H} (T_f - T_{si}) - \frac{F_w}{\rho_i L}. \quad (9)$$

380 Equation (9) defines the thermodynamic growth function, f , found in Eq. (1) and is equivalent to Eq. (1) when dynamic growth is neglected. There are three assumptions inherent to this relationship (Lepparanta, 1993). First, heat conduction in the horizontal direction is assumed to be negligible. Second, it is assumed that there is no thermal inertia present in the ice.

This means that the local derivative of temperature with respect to sea ice depth is constant throughout the sea ice layer and the layer—i.e., the temperature profile is linear—and the system is in equilibrium. The spatial derivative of temperature found

385 in a typical heat equation reduces to the temperature difference between the snow-ice snow-ice interface temperature and the freezing point of water due to these first two assumptions. Next, it is assumed that there is no internal heat source, such as the absorption of short wave radiation. This is The second and third assumptions are only valid during polar winter and times of the year when solar incidence angles are very shallow. Last, heat flux from the sea water to the sea ice is assumed negligible. A more detailed mathematical development of Stefan's Law than the following can be found in Lepparanta (1993).

390 Equation 8 defines the thermodynamic growth function, f , found in Equation 1 and is equivalent to Equation 1 when dynamic growth is neglected. Equation 8 is a differential equation Eqs. (8) and (9) are differential equations with the following analytical

solution (Lepparanta, 1993) solution:

$$H^2 = H_0^2 + a^2 S \sqrt{H_0^2 + \delta t \frac{2\kappa_{eff}}{\rho_i L} (T_f - T_{si})} - \delta t \frac{F_w}{\rho_i L}, \quad (10)$$

where a is defined as

395 $a = \sqrt{\frac{2\kappa_i}{\rho_i L}},$

H_0 is the initial sea ice thickness and S is the sum of negative degree-days and is defined as

$$S = \int_0^t [T_f - T_{si}(\tau)] d\tau.$$

The time interval δt chosen for the results shown herein is one day based on the daily availability of snow-ice interface temperature. The value for a is taken to be $3.3 \text{ cm} (\text{ }^\circ\text{C}^{-1} \text{ d}^{-1})^{1/2}$ (Lepparanta, 1993). This equates to a density of 900 kg m^{-3} , a latent heat of fusion of $3.35 \times 10^5 \text{ J kg}^{-1}$ and a thermal conductivity of $1.9 \text{ W m}^{-1} \text{ K}^{-1}$. The freezing point of sea water is taken to be $-2 \text{ }^\circ\text{C}$ and both snow-ice interface temperature and basal flux are assumed to be constant during each day.

At each time step, the SLICE determines sea ice thickness after thermodynamic growth is determined by solving Equation (4) by solving Eq. (10) for H given an H_0 using the snow-ice interface temperature calculated at the nearest AMSR-E or AMSR2 grid cell. Because both H and H_0 are squared in Equation (4) while the other terms are not, the change in sea ice thickness at each time step is dependent on initial sea ice thickness. This necessitates this retrieval method SLICE be applied in a Lagrangian sense as the sea ice thickness must be tracked and stored in order to accurately calculate the change at the next time step. Fortunately, this mathematical characteristic also means this method is self-correcting. In equation (4) (In Eq. (9)), thicker sea ice grows slower than thinner sea ice and thinner sea ice grows faster than thicker ice with a given snow-ice interface temperature. This means that in the presence of only thermodynamic effects, sea ice that is too thick or too thin will correct towards the true thickness unbiased SLICE thickness profile. This relationship replicates the phenomenon described in Bitz and Roe (2004), whereby thick ice grows slower than thin ice and vice versa.

3.2.2 Basal flux

Observation of basal flux from liquid sea water to solid sea ice is inherently difficult. Typically, basal flux is calculated as a residual of other more readily observed quantities in the heat budget of a one-dimensional sea ice profile, typically from a drifting station or buoy. Using this methodology, McPhee and Untersteiner (1982) observed March through May basal fluxes of less than 2 W m^{-2} using data from the FRAM I drift station in the Arctic Ocean. Perovich and Elder (2002) report oceanic heat flux values of just a few W m^{-2} from November to May during the Surface Heat Budget of the Arctic Ocean (SHEBA) field experiment and Lei et al. (2014) examined Chinese National Arctic Research Expedition (CHINARE) buoy data to discover relatively high basal ocean heat fluxes of greater than 10 W m^{-2} through December that gradually decreased to near 0 by mid-February.

425 Maykut and Untersteiner (1971) completed a sensitivity analysis using their thermodynamic sea ice model, investigating the equilibrium mean annual sea ice thickness corresponding to basal flux values ranging from 0 to 8 W m⁻². Realistic mean annual sea ice thickness resulted when basal flux was set between 1.3 W m⁻² and 2.6 W m⁻². They chose a constant basal flux value of 2 W m⁻² for their model based on this analysis and available observational data. The coupled ocean–sea ice model PIOMAS supplies oceanic heat fluxes to the sea ice model component as modeled by the ocean model component. Zhang and Rothrock (2003) show these modeled ocean heat fluxes in most of the Arctic basin to be near 2 W m⁻². K21 also employed a constant basal heat flux of 2 W m⁻².

430 In keeping with these studies, we apply a constant basal oceanic heat flux $F_w = 2 \text{ W m}^{-2}$. The effect of basal oceanic heat flux on thermodynamic sea ice growth is independent of thickness and can be easily quantified as the last term of Eq. (10). For a given snow–ice interface temperature, the reduction of sea ice thickness growth by inclusion of a basal flux is linearly related to the basal flux value by a factor of $1/\rho_i L$. With a density of 917 kg m⁻³ and a latent heat of fusion of $3.32 \times 10^5 \text{ J kg}^{-1}$, each 1 W m⁻² of basal flux from the liquid sea water to solid sea ice decreases sea ice thickness growth by $2.84 \times 10^{-4} \text{ m d}^{-1}$. Removal of the 2 W m⁻² basal oceanic heat flux would increase sea ice growth by $5.67 \times 10^{-4} \text{ m d}^{-1}$ and an increase from 2 W m⁻² to 10 W m⁻² would decrease thermodynamic sea ice thickness growth by $2.27 \times 10^{-3} \text{ m d}^{-1}$. This corresponds to a 435 0.0857 m increase and a 0.343 m decrease, respectively, when summed from 1 November to 1 April.

3.2.3 Multi-phase properties of sea ice

440 Sea ice is best described not as a homogeneous solid media but rather as a heterogeneous, multi-phase material including solid ice and pockets of liquid brine whose size and salinity change with varying ice temperatures. In turn, these brine pocket changes significantly affect the bulk thermodynamic properties of the ice layer (Feltham et al., 2006). Equation (10) includes effective thermal conductivity, κ_{eff} , a property that is subject to this effect. As such, we adopt the parameterization of effective conductivity described in Feltham et al. (2006).

We begin by defining a constant ocean salinity, S , of 33 ppt. Next, we will assume that the ice is in thermal equilibrium relative to phase change between liquid brine and solid ice and calculate freezing point temperature (in °C), T_f , as a function of salinity (in ppt) per Notz (2005):

$$445 \quad T_f(S) = -0.0592S - 9.37 \times 10^{-6}S^2 - 5.33 \times 10^{-7}S^3. \quad (11)$$

The latent heat of fusion for liquid to solid phase change is defined as the difference between the enthalpies of the two states. In this case, we will use a latent heat of fusion (in J kg⁻¹), L as calculated as a function of temperature (in °C) by Notz (2005):

$$L(T_f) = 333700 + 762.7T_f - 7.929T_f^2. \quad (12)$$

450 We then use Eq. (15) from Feltham et al. (2006) to define effective thermal conductivity (in $\text{W m}^{-1} \text{K}^{-1}$) as function of sea ice temperature, T_i and sea ice salinity, S_i :

$$\kappa_{eff} = \kappa_{bi} - (\kappa_{bi} - \kappa_b) \frac{(T_f(0) - T_f(S_i))}{(T_f(0) - T_i)}, \quad (13)$$

where κ_{bi} is the thermal conductivity of bubbly ice and κ_b is the thermal conductivity of liquid brine and are defined per Schwerdtfeger (1963), Batrak et al. (2018) and Bailey et al. (2010) (all in $\text{W m}^{-1} \text{K}^{-1}$):

455 $\kappa_{bi} = \kappa_i(2\kappa_i + \kappa_a - 2V_a(\kappa_i - \kappa_a))/(2\kappa_i + \kappa_a + 2V_a(\kappa_i - \kappa_a)) \quad (14)$

$$\kappa_b = 1.162(0.45 - 1.08 \times 10^{-2}T + 5.04 \times 10^{-5}T^2) \quad (15)$$

$$\kappa_i = 1.162(1.905 - 8.66 \times 10^{-3}T + 2.97 \times 10^{-5}T^2) \quad (16)$$

$$\kappa_a = 0.03 \quad (17)$$

$$V_a = 0.025, \quad (18)$$

460 where κ_i is the thermal conductivity of pure ice, κ_a is the thermal conductivity of air and V_a is the fractional volume of air in the sea ice. We will use effective conductivity calculated with surface conditions for SLICE which is similar to the approach adopted by Cox and Weeks (1988) who also used conductivity calculated from the surface to determine conductive flux through the ice layer.

A first-year sea ice (FYI) density of 917 kg m^{-3} and multi-year sea ice (MYI) density of 882 kg m^{-3} was reported by 465 Alexandrov et al. (2010) and these values have seen use in the sea ice thickness calculations from CryoSat-2 data (Laxon et al., 2013; Tilling et al., 2018; Hendricks and Ricker, 2020; Kwok and Cunningham, 2015). A sea ice density of 915 kg m^{-3} is also in use with altimeter data (Kurtz et al., 2014b; Petty et al., 2020) and a sea ice density of 925 kg m^{-3} has been used with IceSat data (Kwok and Rothrock, 2009). Choice of sea ice density is a significant source of uncertainty in altimeter-based estimates of sea ice thickness. Kurtz et al. (2014b) report that the range of densities from 882 kg m^{-3} to 925 kg m^{-3} yields a 1.1 m range 470 in sea ice thickness estimates from a 60 cm snow—ice freeboard with 35 cm of snow. The SLICE system of equations uses a FYI sea ice density of 917 kg m^{-3} . For a given snow—ice interface temperature, basal flux and sea ice thickness, a change to 915 kg m^{-3} would increase sea ice thickness growth rate by at most only 0.2% and a change to 925 kg m^{-3} would decrease sea ice thickness growth by at most only 0.8% .

3.3 Parcel tracking of advection

475 The divergence term on the right hand side of Eq. (1) represents sea ice dynamics and includes the effects of both advection and deformation on local sea ice thickness. Advection moves sea ice parcels horizontally and deformation redistributes sea ice volume vertically through ridging or leading.

The advection effects contained within the divergence term can be approximated using a parcel tracking approach, allowing for the modelling of basin-wide results. This parcel tracking methodology is initialized with the CS2SMOS data from the first

480 week of November and each 25 km x 25 km grid cell is divided into 5 km x 5 km parcels, which are advected daily throughout
the winter using the Polar Pathfinder motion vectors interpolated to their position. This parcel tracking methodology is similar
to the Sea Ice Tracking Utility (SITU, <http://icemotion.labs.nsidc.org/SITU/>) described by DeRepentigny et al. (2016). Each
485 parcel adds sea ice thickness thermodynamically using the SLICE thermodynamic model. At any given time step, the parcels
can be gridded to the EASE-Grid 2.0 by taking the mean thickness of parcels within each grid cell. This approach leaves out
deformation effects. While taking the sum of all parcel volume within each grid cell and dividing by grid cell area would be a
more physically sound methodology for this regridding, the results from such a method proved unrealistic. Figure A2 found in
the Appendix shows a comparison between the chosen method using grid cell mean and the method using grid cell sum. New
parcels are initiated at any grid cell not containing a sea ice parcel but showing 95% or greater sea ice concentration. New ice
490 parcels are initialized at 0.05 m. Any parcel that is located in a region with less than 95% sea ice concentration at any time
step is removed. The result is a daily gridded Arctic basin-wide sea ice thickness dataset representing thermodynamic sea ice
growth in the 95% sea ice concentration ice pack.

4 Results

The SLICE sea ice thickness retrieval methodology can be applied on a single one-dimensional profile basis or across a large
area. Here we present results comparing one-dimensional profiles to ice mass balance buoy thicknesses and Arctic basin-wide
495 results compared to [OIB](#) and [AWI CS2SMOS](#) and [PIOMAS](#) data.

4.1 One-dimensional Profiles

The SLICE retrieval method results were compared to sea ice thickness from ice mass balance buoys. The retrieval method was
initialized with the buoy observed sea ice thickness on ~~the day when the 14 d rolling average sea ice growth exceeded 1 mm~~
~~d⁻¹. From this time step forward, the November and integrated through 1 April. The~~ retrieval method is dependent only on
500 the satellite based snow–ice interface temperature. The snow–ice interface temperature used on a given day is taken from the
nearest AMSR-E or AMSR2 grid cell to the buoy location. The resultant sea ice thickness ~~profiles and buoy profiles are plotted~~
~~in Figure~~ time series are plotted with buoy sea ice thickness in Fig. 3. It is clear from ~~Figure~~ Fig. 3 that the SLICE profiles agree
well with the buoy sea ice thickness when initialized with an accurate initial ice thickness. The correlation coefficients ranges
from ~~0.965 0.37~~ to 0.999 with a mean of ~~0.991 0.88~~ and standard deviation of ~~0.04 0.21~~ across all buoys. The bias, calculated
505 by taking the mean over the entire profile length of the retrieval method result minus the buoy thickness, ranges from ~~-0.078~~
~~m to 0.132~~ ~~-0.01 m to 0.19~~ m with a mean of ~~0.008 0.08~~ m and standard deviation of ~~0.059 0.07~~ m across the buoys. ~~The bias~~
~~grows with time as the SLICE profile moves away from its initialized thickness.~~

~~Ice thickness observations from ice mass balance buoys and SLICE for buoys (a) 2003C, (b) 2005F, (c) 2006C, (d) 2012G,~~
~~(e) 2012H, (f) 2012L, (g) 2013F, (h) 2013Fb, (i) 2013G and (j) 2015F. Linear correlation (r) and bias values are listed. Across~~
510 ~~all buoys, the r values have a mean of 0.991 and the biases have a mean of 0.008 m.~~

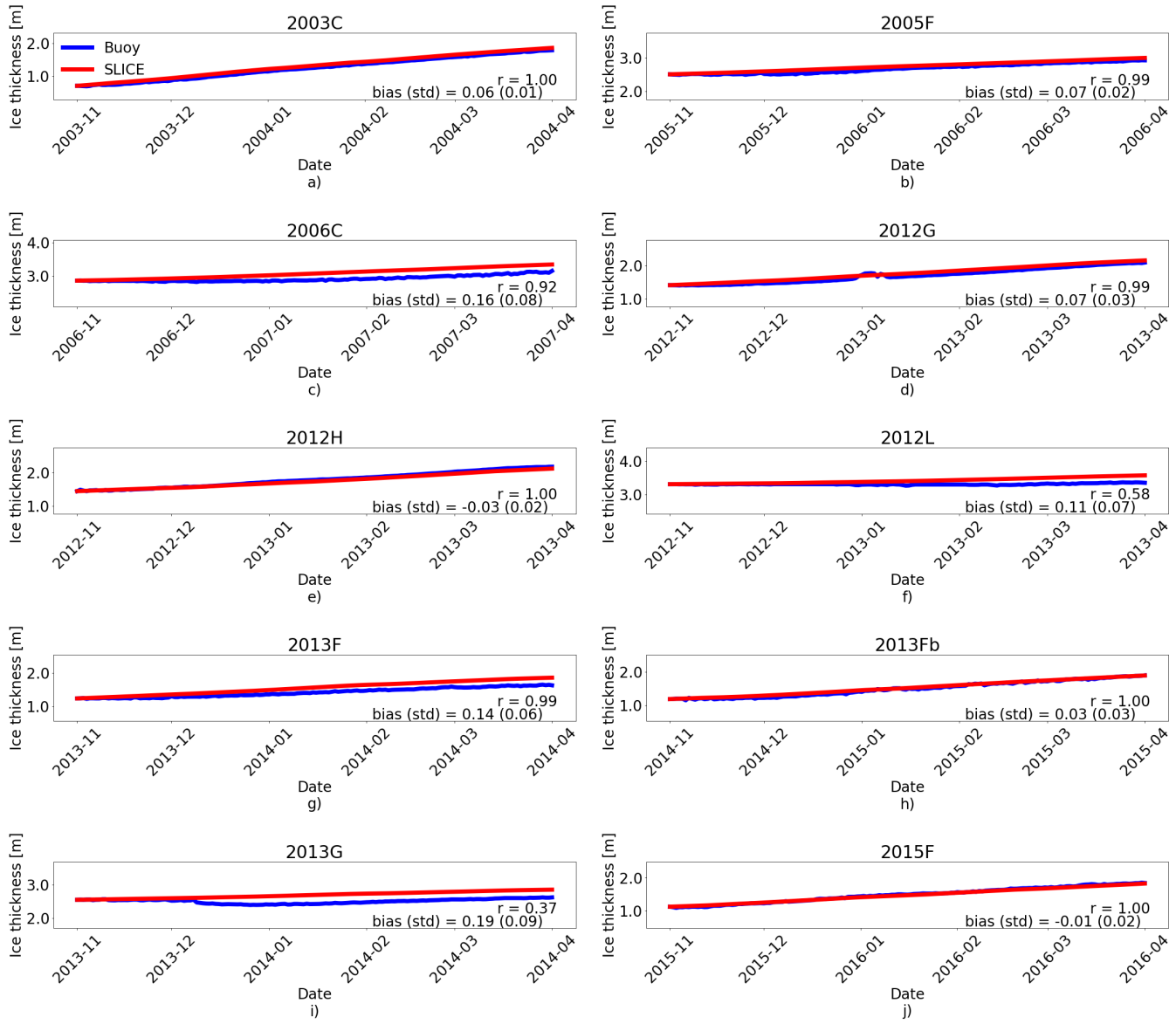


Figure 3. Ice thickness observations from ice mass balance buoys and SLICE for buoys (a) 2003C, (b) 2005F, (c) 2006C, (d) 2012G, (e) 2012H, (f) 2012L, (g) 2013F, (h) 2013Fb, (i) 2013G and (j) 2015F. Linear correlation (r) and bias values are listed. Across all buoys, the r values have a mean of 0.88 and the biases have a mean of 0.08 m.

4.2 Arctic Basin-wide Comparisons

The initial condition is very important for the accuracy of sea ice thickness SLICE retrieval method. At the same time, due to the dependency of sea ice growth on initial thickness shown in Equation 8, an initial condition that is biased high will lead

to a lower growth rate and an initial thickness that is biased low will lead to a higher growth rate. In this way, SLICE is self-correcting. In Figure ??, the retrieval method is initialized with sea ice thickness that is 0.25 m both higher and lower than the buoy thickness. The profiles follow the same smooth thermodynamic growth exhibited in Figure 3 and both approach the buoy sea ice thickness over time.

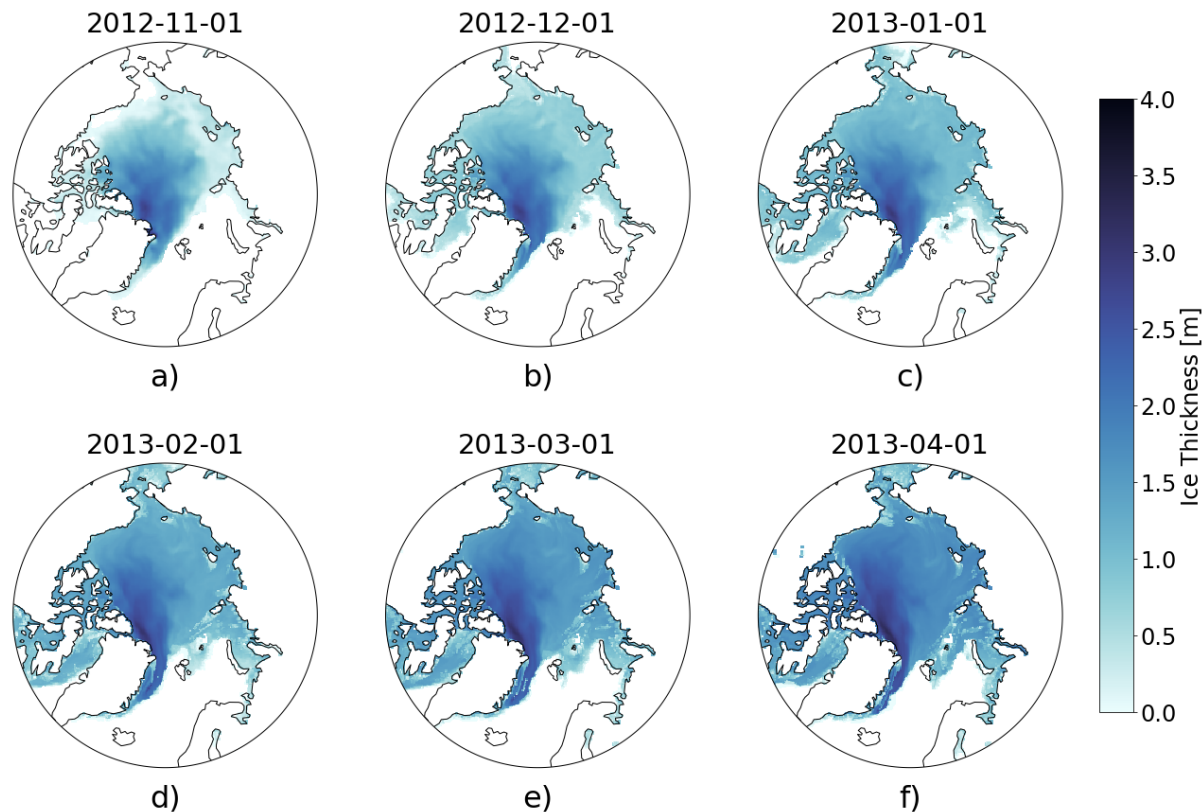


Figure 4. Ice thickness observations from Sea ice mass-balance buoys and sea ice thickness on a) 2 November 2012, b) 1 December 2012, c) 1 January 2013, d) 1 February 2013, e) 1 March 2013, f) 30 April 2013 created using SLICE retrieval method for buoy 2013Fb with shading bounded by the retrieval method initialized at ± 0.25 m 1 November 2012 AWI CS2SMOS as an initial state. The higher changes from month to month represent thermodynamic growth and lower initialized profiles both approach the bold retrieval method profile with accurate initial condition over time advection.

4.3 Arctic Basin-wide Comparisons

Next, the SLICE retrieval method was applied utilized to model sea ice thickness on a Arctic basin-wide scale. Using the 520 AWI CS2SMOS data for the first week of November as the initial state for one set of integration and the PIOMAS data from 1 November as the initial state for another set of integration, the retrieval method was applied daily to the entire Arctic basin from November to 1 November to 1 April for the growth seasons beginning in 2012 through 2019. November first was chosen

to ensure most ice was below the freezing point and there were limited melt ponds to interfere with the snow ice interface temperature observation. Only grid cells with 95% or greater sea ice concentration are considered, again to ensure accuracy of the snow ice interface temperature. The basin-wide results are on the 25km. At each time step, the parcel tracking methodology described in Sect. 3.3 is applied. The 1 April results are regridded to the 25 km EASE-Grid 2.0. The AWI CS2SMOS data are on the same grid and the PIOMAS data are linearly interpolated from its native grid to the 25km EASE-Grid 2.0. The result is a daily gridded Arctic basin-wide sea ice thickness dataset representing thermodynamic sea ice growth in the 95% sea ice concentration ice pack for the sea ice growth seasons beginning in the years 2012 to 2019. If at a given time step the AMSR-E and AMSR2 SIC product shows there is sea ice in a grid cell but the method does not, new ice is initialized at 0.05m. All ice motion is neglected in the creation of this dataset.

Sea ice thickness on a) 2 November 2012, b) 1 December 2012, c) 1 January 2013, d) 1 February 2012, d) 1 March 2013, e) 1 April 2013, f) 30 April 2013 created using SLICE with the November 1st, 2012 AWI CS2SMOS as an initial state. The overall structure changes little, as only thermodynamics are captured.

using the procedure also described in Sect. 3.3. Monthly basin-wide sea ice thickness plots for the sea ice growth season beginning in fall 2012 using AWI CS2SMOS as the initial state are shown in Figure Fig. 4. The sea ice thickness data from SLICE is available daily. The data from but only the first of every month is plotted. The sea ice thickness on 30 April 2013 is higher but shows similar spatial distribution to that on 2 November 2012. The sea ice is growing thermodynamically but there is no dynamics to rearrange the thickness distribution is increasing and advection is relocating the volume horizontally throughout the Arctic basin.

The cumulative effects of this lack of dynamics are depicted in Figures ?? and ?? which each compare In order to compare SLICE with PIOMAS and K21 data, all three datasets were compared with OIB sea ice thickness from SLICE to a reference dataset at the end of each growth season beginning in 2012 through 2019. Figure ?? compares SLICE to AWI CS2SMOS and Figure ?? compares SLICE with PIOMAS data observations. OIB data from the month of March for the years 2013 through 2018 (including NSIDC OIB quick looks data) was first binned by 25 km EASE 2.0 grid cell and averaged across each bin to create an OIB dataset collocated with SLICE. Both PIOMAS and the K21 data were also interpolated to the 25 km EASE 2.0 grid. A comparison between SLICE, PIOMAS and K21 was created and shown in Fig. 5. Linear correlation and bias statistics were calculated from this data. All three datasets show very similar linear correlations of 0.67, 0.67 and 0.68 for SLICE, PIOMAS and K21, respectively. The best mean bias is PIOMAS at 0.10 m, followed closely by SLICE at -0.12 and K21 at -0.24 m. The standard deviation of the bias is 0.68 for both PIOMAS and SLICE and nearly the same for K21 at 0.69. The end of the growth season is the week ending 15 April for

SLICE was also compared to PIOMAS using AWI CS2SMOS as the reference dataset. Figure 6 shows the differences in sea ice thickness between SLICE and AWI CS2SMOS and 30 April for PIOMAS. The AWI CS2SMOS and PIOMAS data are a snapshot of the absolute thickness and would therefore capture both thermodynamic and dynamic processes the differences between PIOMAS and AWI CS2SMOS on 1 April for the years 2013 through 2020. Figure A1 in the Appendix shows plots of sea ice thickness used in this comparison from all three datasets. The differences are mostly between -1 m and 1 almost all between -1.5 m and 1.5 m and in most cases are near zero. The pattern exhibited by the differences is what would be

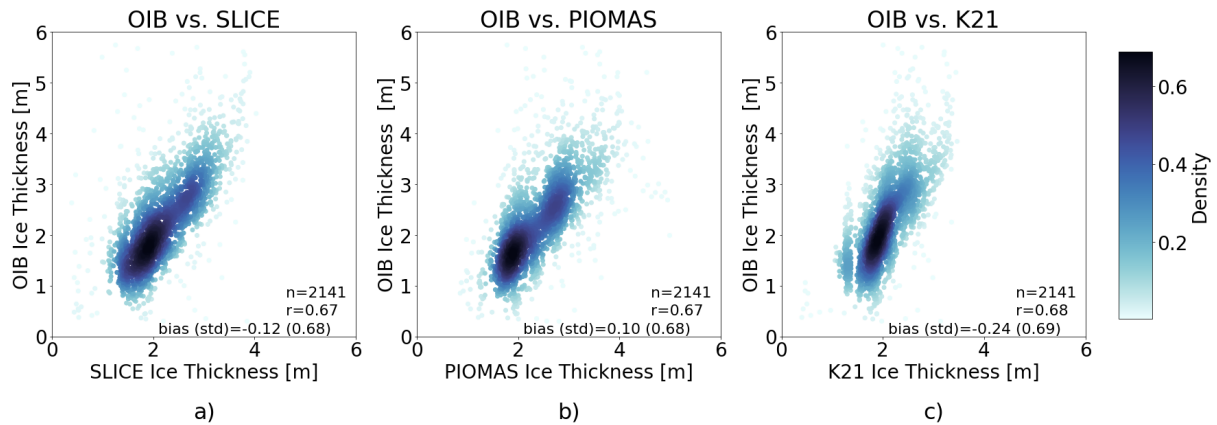


Figure 5. OIB thickness versus a) SLICE initialized with CryoSat-2/SMOS, b) PIOMAS and c) Kang et al., 2021 data including number of data points, linear correlations and bias (standard deviation). SLICE has the highest linear correlation though all three are virtually equal.

expected from a lack of dynamic effects—lower SLICE sea ice thickness where anti-cyclonic flow pushes ice to the north of the Canadian Archipelago, lower SLICE sea ice thickness where the transpolar drift pushes ice to the east of Greenland and higher SLICE sea ice thickness over the marginal seas from which the sea ice moves away after initial growth. Additionally, the SLICE retrieval method overestimates ice thickness in Baffin Bay in all years for both reference datasets, likely difference plots for SLICE and PIOMAS show similar patterns, though PIOMAS overestimates thickness in more areas than SLICE, which underestimates sea ice thickness in the central Arctic in almost all cases. The differences between SLICE and CS2SMOS are likely to be due to a lack of export of ice from this region.

560

565

570

575

Tables ?? and ?? show the total yearly volumetric growth shown by the SLICE retrieval method and the deformation effects. Figure 7 shows a scatter plot of AWI CS2SMOS sea ice thickness to sea ice thickness from SLICE and PIOMAS data respectively and their differences in absolute and relative terms. Only grid cells that contain ice in both SLICE and the reference dataset were considered, likely meaning the marginal ice zone is excluded due to the retrieval method only capturing grid cells with >95% sea ice concentration. In all years, SLICE exceeds the volume growth captured by from PIOMAS. Both AWI CS2SMOS .Following the growth season beginning in 2013, SLICE only exceeded the AWI and SLICE are on a 25 km EASE-Grid 2.0 but in order to compare the AWI CS2SMOS volume growth by 4.2% of the data to PIOMAS, it is interpolated to each PIOMAS grid point. Linear correlation and bias statistics were calculated from this data. SLICE and PIOMAS have equal linear correlations with AWI CS2SMOS growth but in most years SLICE exceeds the at 0.77. SLICE shows an improved mean bias at 0.03 m compared to PIOMAS at 0.10 m. SLICE standard deviation of the difference is also improved at 0.62 compared to 0.67 m for PIOMAS. Figure 8 shows total daily Arctic sea ice volume from SLICE, PIOMAS and AWI CS2SMOS by over 10%. Following the growth season beginning in during the winters from late 2012 , SLICE exceeds to early 2020. The AWI CS2SMOS is taken from the the weekly data centered on each day. Both SLICE and PIOMAS follow the AWI CS2SMOS

volume growth by 18.1%. The SLICE retrieval method exceeds AWI CS2SMOS in volumetric growth by a mean of 12.0% and a standard deviation of 5.5% in the years 2012–2019.

580 In contrast to in comparison with AWI CS2SMOS, the SLICE retrieval method underestimates volumetric sea ice profile well. PIOMAS overestimates end of season volume in all years and underestimates initial volume in all cases except 2012–2013 and 2016–2017 leading to an overestimation of sea ice volume growth in all years when compared to PIOMAS though the relative differences are reduced. SLICE produces a mean of 8.3% less volumetric growth compared to PIOMAS in the years 2012–2019. The differences are more consistent than in comparison with AWI. SLICE begins each season at the same volume 585 as AWI CS2SMOS with a standard deviation of 2.0%. The maximum difference of 11.7% occurred following the growth season beginning in 2017 and the minimum difference of 5.4% occurred following the growth season beginning in 2015. Again, only grid cells with ice in both datasets are considered and ends all seasons closer than PIOMAS to the AWI CS2SMOS volume except 2014–2015 and 2016–2017. While there are not enough data points for a strong statistical comparison, SLICE is certainly a viable indicator of sea ice volume growth.

590 A comparison of volumetric sea ice growth between PIOMAS and SLICE for the years 2021 through 2020. PIOMAS exceeds SLICE in volumetric growth by a mean of 8.3% and a standard deviation of 2.0%. Winter Season SLICE Volume Growth km³ PIOMAS Volume Growth km³ Difference (SLICE – PIOMAS) km³ Difference / PIOMAS Volume Growth % 2012 14574 15862 1287 -8.1 2013 12590 13738 1148 -8.4 2014 12926 13870 944 -6.8 2015 12518 13233 715 -5.4 2016 12884 13811 926 -6.7 2017 12556 14218 1663 -11.7 2018 13225 14578 1353 -9.3 2019 13867 15364 1496 -9.7

595 5 Discussion

The SLICE retrieval method captures SLICE uses a new retrieval of snow–ice interface temperature (Lee and Sohn, 2015) to drive a very simple one-dimensional model of sea ice thermodynamics in order to retrieve thermodynamic sea ice thickness 600 aceretion very well. growth. By applying SLICE to individual parcels whose location throughout the Arctic basin is determined using a sea ice motion product (Tschudi et al., 2020), SLICE is able to capture sea ice advection and produce basin-wide results. In doing so, SLICE functions similarly to much more intricate sea ice models such as PIOMAS (Zhang and Rothrock, 2003) and a sea ice model that is nudged with retrieved snow–ice interface temperature (Kang et al., 2021). While SLICE is capable of capturing thermodynamic sea ice growth and advection, it is unable to detect deformation effects—i.e., thickness changes due ridging or leading.

Figure 3 shows a comparison between ice mass balance buoy sea ice thickness measurements and the retrieval method 605 initialized with the buoy data for 10 buoys within the years 2003–2016. The mean correlation coefficient of 0.991 0.88 between the buoy measurements and the method is high. The bias values are also very encouraging with a mean of 0.008 m. 0.08 m. Buoys 2012L and 2013G have linear correlation values of 0.58 and 0.37, respectively, both significantly lower than the others. These buoys may have experienced delayed ice growth that begins later than 1 November or perhaps even melting. SLICE 610 is unable to capture either phenomena, degrading the results from these buoys. The median linear correlation across all buoy results is 0.992 and the mean linear correlation from all buoys except 2012L and 2013G is 0.985. When sea ice is indeed

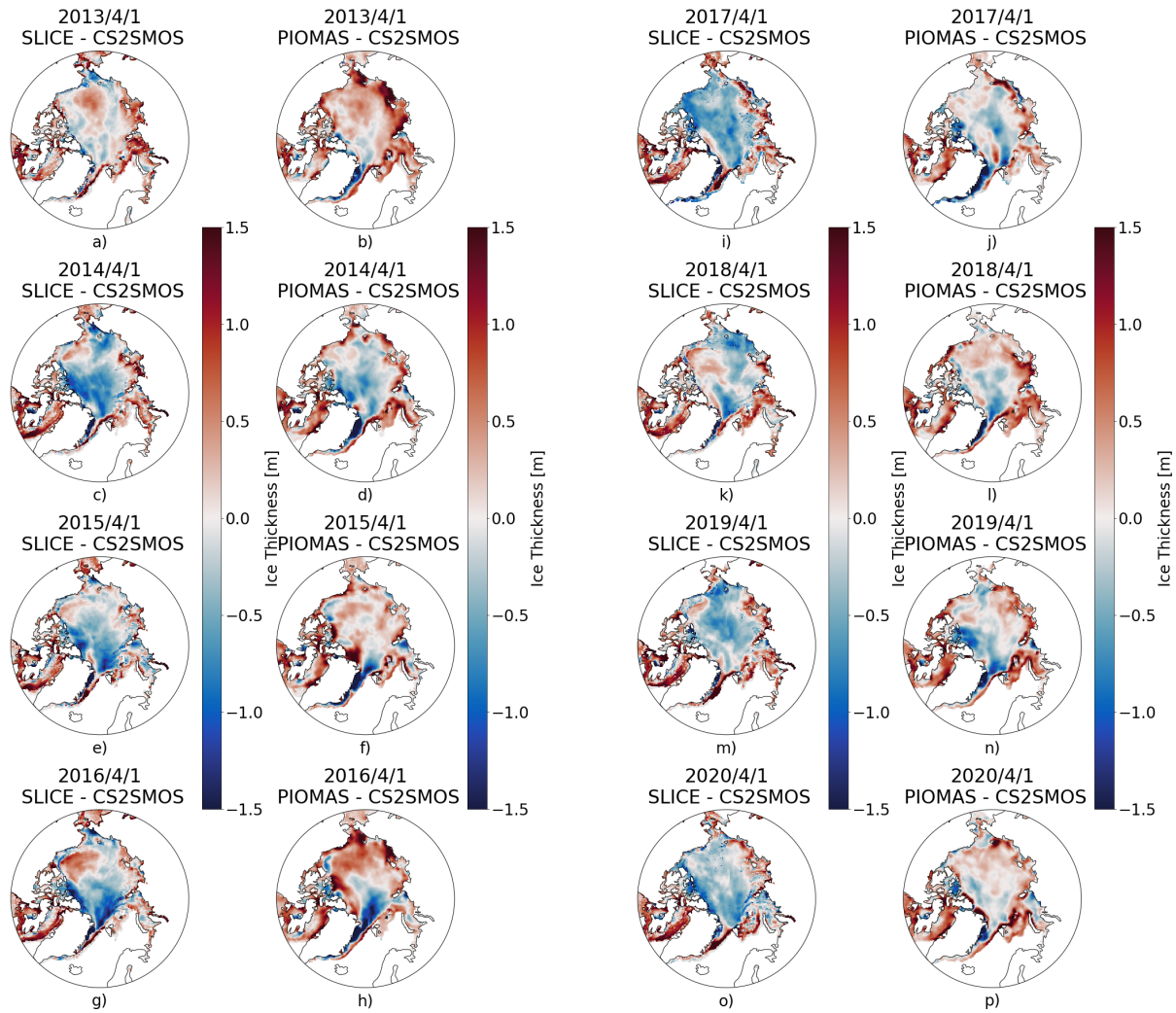


Figure 6. For the sea ice growth seasons ending in a–ca–b) 2013, d–fc–d) 2014, g–ie–f) 2015, j–lg–h) 2016, m–ei–j) 2017, p–rk–l) 2018, s–um–n) 2019 and v–xo–p) 2020, a, c, e, g, i, k, m, o) SLICE initialized with sea ice thickness - AWI CS2SMOS sea ice thickness from the first week of November 1 April and b, d, f, h, j, l, n, p) PIOMAS sea ice thickness - AWI CS2SMOS sea ice thickness and their difference on 15 from 1 April. Their differences represent dynamic changes. The SLICE and are PIOMAS differences show similarities in areas expected by climatology their overall pattern.

increasing via thermodynamics, SLICE captures the growth well. Additionally, SLICE has a self-correcting quality by nature of Equation 8 Eq. (9) whereby sea ice thicknesses that are biased in either direction approach the correct unbiased SLICE sea ice thickness over time as shown in Figure ???. These points suggest the retrieval method is viable as a basis for estimating modelling sea ice thickness but is highly dependent on an initial condition, as it calculates thermodynamic sea ice thickness

615 increase rather than absolute thickness.

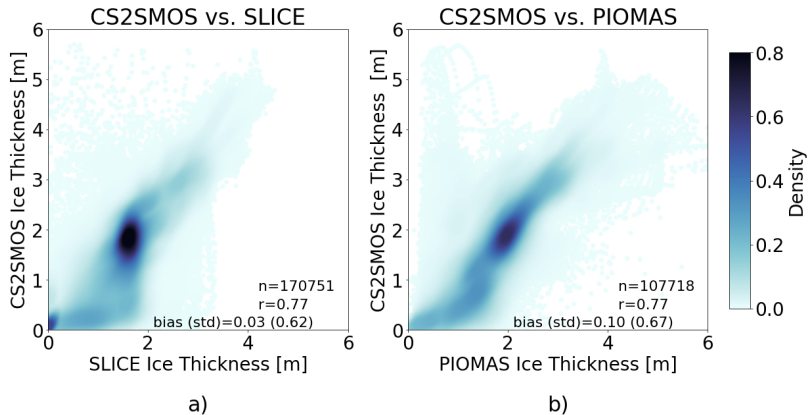


Figure 7. A comparison of volumetric sea ice growth between AWI CS2SMOS and SLICE for the years 2021 through 2019. SLICE exceeds AWI CS2SMOS in volumetric growth by sea ice thickness versus a) mean SLICE sea ice thickness and b) PIOMAS sea ice thickness including number of 12.0% data points, linear correlations and α -bias (standard deviation of 5.5%). SLICE has as lower bias at 0.03 m than PIOMAS at 0.10 m and linear correlation values are equal.

Winter Season SLICE Volume Growth km^3 CS2SMOS Volume Growth km^3 Difference (SLICE - CS2SMOS) km^3 Difference/CS2SMOS Volume Growth % 2012 13990 11849 2141 18.1 2013 11912 11433 478 4.2 2014 12479 11455 1024 8.9 2015 12102 10315 1787 17.3 2016 11962 11384 578 5.1 2017 11892 10386 1506 14.5 2018 12452 10677 1775 16.6 2019 13177 11790 1397 11.8

While SLICE is capable of retrieving thermodynamic sea ice growth, it is unable to detect dynamic effects—i.e., thickness changes due to ice motion. Figure 4 shows monthly basin-wide plots of sea ice thickness for the sea ice growth season beginning on 1 November 2012 created using the retrieval method with an initial condition provided by the AWI CS2SMOS dataset. The sea ice thickness values are greater but the spatial distribution is similar from month to month as parcels are not moving, rather 620 only growing thermodynamically. The consequences of this lack of dynamic sea ice thickness change are explored in Figures ?? and ?? showing basin-wide comparisons of sea ice thickness from SLICE to that from AWI CS2SMOS and PIOMAS, respectively. The AWI CS2SMOS and PIOMAS products both have thicker ice in regions where dynamic sea ice effects are expected to increase ice thickness, notably north of the Canadian Archipelago and east of Greenland, and thinner ice in the 625 marginal seas from where ice is exported. The difference plots between SLICE and these reference datasets look similar in each year. These plots are integrated to a volume perspective in Tables ?? and ?? . In all cases, SLICE is within 20% volumetric growth of the reference dataset. Interestingly, the retrieval method shows greater volumetric growth than CS2SMOS in all years and less volumetric growth than PIOMAS in all years.

These results are encouraging for the capability of SLICE to capture volumetric sea ice changes on a basin-wide scale. Per the model described by Equation 1, sea ice volume is only added through thermodynamic processes—dynamic 630 processes only serve to rearrange the volume already present. Though this statement does invoke the false assumption that dynamic processes do not change the density of the ice, it seems to be a factor in explaining the volumetric results described in Tables ?? and ?? . Though dynamic processes do not directly change sea ice volume, their changing of the thickness of ice at a

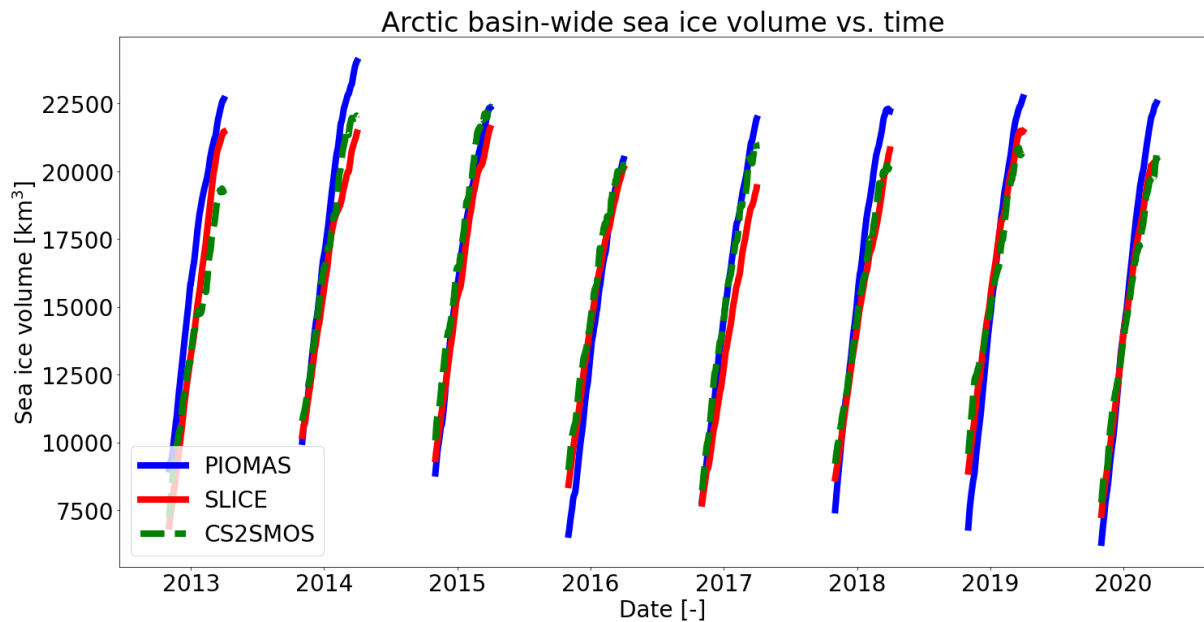


Figure 8. For the Wintertime sea ice growth seasons ending in a–e) 2013, d–f) 2014, g–i) 2015, j–l) 2016, m–o) 2017, p–r) 2018, s–u) 2019 and v–x) 2020, volume versus time for SLICE initialized with PIOMAS on 1 November, PIOMAS sea-ice thickness and their difference on 15 April AWI CS2SMOS. Their differences represent dynamic changes and are in areas expected by climatology.

given location does impact thermodynamic processes by virtue of f being a function of thickness, H , in Equation 1. Inspection of Equation 8 indeed shows that H impacts $\frac{\partial H}{\partial t}$. In regions where dynamic processes increase sea ice thickness, SLICE will overestimate sea ice thickness increase and in regions where dynamics decrease sea ice thickness, it will underestimate sea ice thickness increase. These phenomena, along with any phenomena inherent to either reference dataset, may explain volumetric differences between SLICE and the reference datasets.

Another potential factor explaining differences in volumetric growth of SLICE versus the reference datasets is the choice of sea ice growth start and end dates. Figure 3 shows that most buoys experience sea ice thickness growth beginning around 1 November. November first is also the start date for the basin-wide growth examples shown in Figures 4, ?? and ?? but this is undoubtedly inaccurate for some of the Arctic basin, regions of which begin ice accretion at varying start dates based on local conditions. Additionally, SLICE is incapable of capturing ice melt. If at any time during the growth season a region were to experience melting, the associated ice thickness decrease would not be captured. SLICE results are dependent on the values provided for the freezing point of sea water, thermal conductivity, density and latent heat, all of which are not constant values across the Arctic as we have treated them here. An additional value that is influential for the retrieval method is the initial 0.05 m ice given to grid cells where the SIC dataset shows new ice. A more rigorous treatment of these constants and their variation across the basin may improve the results.

There are a number of assumptions inherent to Stefan's Law (Lepparanta, 1993) that must be considered in relation to SLICE ~~as introduced in Sect. 3.2.~~ In order to characterize conduction through the ice layer with only the snow–ice interface 650 temperature and an assumed freezing point temperature at the bottom of the ice layer, it must be assumed that heat conduction in the horizontal is negligible and that the local vertical derivative of temperature throughout the ice layer is constant. These assumptions are reasonable. The remaining two assumptions are more salient. The first is that there is no internal heat source. This is untrue when there is significant short wave radiation absorbed within the sea ice. The final assumption is that ~~there is no~~ heat exchange between the sea ice and the ocean ~~is constant in space and time~~, which is likely to be invalid in some regions.

655 Impacts of this assumption on the sea ice growth are investigated in Sect. 3.2.2.

Another source of uncertainty in SLICE ice thickness is the constraint that it is limited to areas with sea ice concentration greater than 95%. There is significant growth in areas where the sea ice concentration is low, such as the marginal ice zone (MIZ). This constraint would likely cause underestimated sea ice growth over those areas. In a supplement to the body of the 660 paper, Lee and Sohn (2015) suggest a procedure for calculating snow–ice interface temperature in areas with less than 95% but that has not been implemented here, pending further investigation. Further validation of SLICE, particularly in regions other than the Beaufort Sea and Central Arctic, where all ~~ten buoys~~ ~~buoys and OIB flights~~ used here were located, as well as investigation of the impacts of these assumptions and full characterization of uncertainties is warranted.

The ~~SLICE retrieval method uses passive microwave brightness temperatures from the AMSR-E and AMSR2 instruments and a Stefan's Law energy balance relationship and attendant assumptions amounts to a simplification the multi-layer thermodynamic model based on Maykut and Untersteiner (1971) that makes up the foundations of PIOMAS and K21. These assumptions remove the need for multiple layers. Additionally, whereas the thermodynamics in PIOMAS and K21 are driven by an atmospheric reanalysis product and nudged by snow–ice interface temperature retrieval algorithm (Lee and Sohn, 2015) to drive a sea ice thickness growth equation. Gridded brightness temperature data from these instruments are available at daily temporal resolution in the polar regions (Cavalieri et al., 2014; Markus et al., 2018), meaning daily sea ice thickness growth is available basin-wide. Lee et al. (2018) provides a method for retrieving in the case of K21, SLICE is driven by satellite observed snow–ice interface temperatures using passive microwave brightness temperatures from the SSM/I and SSMIS instruments, allowing for the application of SLICE to sea ice growth seasons beginning in 1987. Current state of the art temperature. These factors allow for the instantaneous retrieval of thermodynamic thickness growth rate. Whereas PIOMAS models sea ice motion again using atmospheric reanalysis, SLICE uses a sea ice motion satellite product when used to model basin-wide sea ice thickness observations from space, though capable of observing sea ice growth whether from thermodynamic or dynamic effects, are not capable of this spatial and temporal coverage. They also do not discriminate between dynamic and thermodynamic effects. For these reasons, a~~. This sea ice motion product and the snow–ice interface temperature product mean SLICE is heavily observationally constrained. The comparison between SLICE, PIOMAS and K21 show that these assumptions and simplifications do not degrade resultant sea ice thickness dataset based on SLICE will be especially qualified for investigating thermodynamic and dynamic sea ice phenomena that are small scale in space and time. SLICE need not be initialized the beginning of the growth season and applied for an entire growth season but can be initialized at any time during the growth season and applied to any interval of time, allowing for use with case studies or other small time and space

scale events. Additionally, the high temporal resolution retrieval of thermodynamic effects will allow for creation of useful datasets of surface energy flux from latent heat of fusion. Lastly, we are aware of no reason SLICE could not also be applied to Antarctic sea ice or freshwater bodies—values when SLICE thermodynamic growth rate is used to model absolute thickness on a basin-wide scale, even without a deformation component.

With the availability of sea ice motion observation datasets from NSIDC (Tschudi et al., 2020) and the European Organisation for the Exploitation of Meteorological Satellites (EUMETSAT) Ocean and Sea Ice Satellite Application Facility (OSISAF) (Lavergne et al., 2010), there is potential to add a dynamic component to SLICE by solving the second term of Equation 1. Much effort has gone into discretizing this term for use with numerical techniques. A discussion of solution schemes for this type of equation as it relates to sea ice transport is found in Lipscomb and Hunke (2004). An ideal scheme must conserve volume, must be stable, must be second-order accurate in space in order to avoid excessive diffusion, preserve monotonicity and be efficient. Early climate models utilized the multidimensional positive-definite advection transport algorithm (MPDATA) introduced in Smolarkiewicz (1984). The current iteration of the Los Alamos sea ice model (CICE) solves these types of transport equations using an incremental remapping scheme (Hunke and Lipscomb, 2010; Lipscomb and Hunke, 2004). Numerical solution schemes such as these for solving the second term in Equation 1 are under consideration for use with this retrieval method but are beyond the scope of this present work. If a suitable dynamic component can be developed, a climatology of both thermodynamic and dynamic Figure 8 is encouraging for the capability of SLICE to capture volumetric sea ice changes on a basin-wide scale. Per the model described by Eq. (1), sea ice volume is only added through thermodynamic processes—dynamic processes only serve to rearrange the volume already present. Though this statement does invoke the false assumption that dynamic processes do not change the density of the ice, it seems to be a factor in explaining the volumetric results. Though dynamic processes do not directly change sea ice volume, their changing of the thickness of ice at a given location does impact thermodynamic processes by virtue of f being a function of thickness, H , in Eq. (1). Inspection of Eq. (8) indeed shows that H impacts $\frac{\partial H}{\partial t}$. In regions where deformation increases sea ice thickness, SLICE will overestimate sea ice thickness increase and in regions where deformation decreases sea ice thickness growth will be created. It will underestimate sea ice thickness increase. These phenomena, along with any phenomena inherent to either reference dataset, may explain volumetric differences between SLICE and the reference datasets.

6 Conclusions

New methods for observing snow–ice interface temperature (Lee and Sohn, 2015) have made possible a new strategy for observing thermodynamic sea ice thickness growth from space during the winter growth season: Stefan’s Law Integrated Conducted Energy (SLICE). The new strategy involves coupling observed satellite retrieved snow–ice interface temperature with Stefan’s Law (Stefan, 1891; Lepparanta, 1993). In the Stefan’s Law relationship, latent heat of fusion is conducted from the bottom of the ice layer where new ice forms to the snow–ice interface and this rate of conduction and accretion is calculated using the snow–ice interface temperature and an assumed a parameterized freezing point temperature at the bottom of the ice layer. An initial value is required as SLICE calculates The snow–ice interface temperature retrieval algorithm used to

drive the sea ice thickness growth rather than absolute thickness and does not capture melting. Four assumptions make this relationship possible, including (1) negligible horizontal conduction, (2) no thermal inertia in the ice, (3) no internal heat sources and (4) no heat flux from the sea water equation uses passive microwave brightness temperatures from the AMSR-E and AMSR2 instruments (Lee and Sohn, 2015). Gridded brightness temperature data from these instruments are available at 720 daily temporal resolution in the polar regions (Cavalieri et al., 2014; Markus et al., 2018), meaning modelled daily sea ice thickness growth is available basin-wide. Lee et al. (2018) provides a method for retrieving snow–ice interface temperatures using passive microwave brightness temperatures from the SSM/I and SSMIS instruments, allowing for the application of SLICE to sea ice growth seasons beginning in 1987. SLICE requires an initial sea ice thickness value is required and does not capture melting.

725 When SLICE is initialized with an ice mass balance buoy thickness and compared against that buoy's ice thickness profiles during the ice growth season, the retrieval method compares extremely well with the buoy observed sea ice thickness growth. Using ten buoys from 2003 to 2016, the mean linear correlation value is 0.991–0.88 and the mean bias is 0.008 m. Two sets of 0.08 m. SLICE can be used to model basin-wide integrations were also performed for the winter growth seasons beginning in the years 2012–2020 using an initial state from the sea ice thickness by applying the thermodynamic growth 730 retrieval to individual sea ice parcels and advected the parcels across the basin using a sea ice motion product. This basin-wide methodology was applied to the winters between late 2012 and early 2020 using AWI CS2SMOS and PIOMAS datasets. SLICE underestimated volumetric growth in all years when compared to PIOMAS with a mean of 8.1% in relative difference and overestimated volumetric growth in all years when compared to AWI CS2SMOS with a mean of 11.9% in relative difference. The differences between ice thickness estimated with SLICE, a thermodynamic method, and the reference data follow a pattern 735 expected from the dynamic motion of the ice pack basin-wide sea ice thickness as the initial state. Results show that SLICE performs comparably to PIOMAS and K21, despite the assumptions and simplification that allow for the direct retrieval of instantaneous thermodynamic growth rate.

740 The SLICE retrieval method is only capable of retrieving thermodynamic Current state of the art sea ice thickness observations from space, though capable of observing sea ice growth, which neglects dynamic growth. While a better understanding of thermodynamic growth on its own is useful, a product that also includes dynamic growth would be advantageous to the field. With the availability of ice motion and ice drift satellite products, there is potential for a dynamics component to be paired with the thermodynamic component demonstrated here. With the availability of snow–ice interface temperature beginning in 1987 and ice motion products beginning in 1978, a climatology of daily sea ice thickness, thermodynamic growth and dynamic growth on a basin-wide scale may be possible. Such a dynamic component and climatology are in development whether from 745 thermodynamic or dynamic effects, are not capable of this spatial and temporal coverage. They also do not discriminate between dynamic and thermodynamic effects. For these reasons, a sea ice thickness dataset based on SLICE will be especially qualified for investigating thermodynamic and dynamic sea ice phenomena that are small scale in space and time. SLICE need not be initialized at the beginning of the growth season and applied for an entire growth season but can be initialized at any time during the growth season and applied to any interval of time, allowing for use with case studies or other small time and space

750 scale events. Additionally, the high temporal resolution retrieval of thermodynamic effects will allow for creation of useful datasets of surface energy flux from latent heat of fusion.

Code and data availability. Data used in creation of all figures is available at <https://doi.org/10.5281/zenodo.6554832>. Code for creation of data and figures is available at <https://doi.org/10.5281/zenodo.6561431> and <https://github.com/janheuser/SLICE/releases/tag/1.0.0>. The following auxilliary datasets were used and are available at these locations: AMSR-E and AMSR2 brightness temperatures, https://doi.org/10.5067/AMSR-E/AE_SI25.003 and <https://doi.org/10.5067/TRUIAL3WPAUP>; AMSR-E and AMSR2 SIC, https://doi.org/10.5067/AMSR-E/AE_SI25.003 and <https://doi.org/10.5067/TRUIAL3WPAUP>; AWI CS2SMOS, <https://www.meereisportal.de>; sea ice motion vectors, <https://doi.org/10.5067/INAWUWO7QH7B>; OIB, <https://doi.org/10.5067/G519SHCKWQV6>; CRREL IMB, <http://imb-crrel-dartmouth.org>; PI-OMAS, <http://psc.apl.uw.edu/research/projects/arctic-sea-ice-volume-anomaly>; Kang et al., 2021, <https://doi.org/10.1029/2020MS002448>.

Appendix A

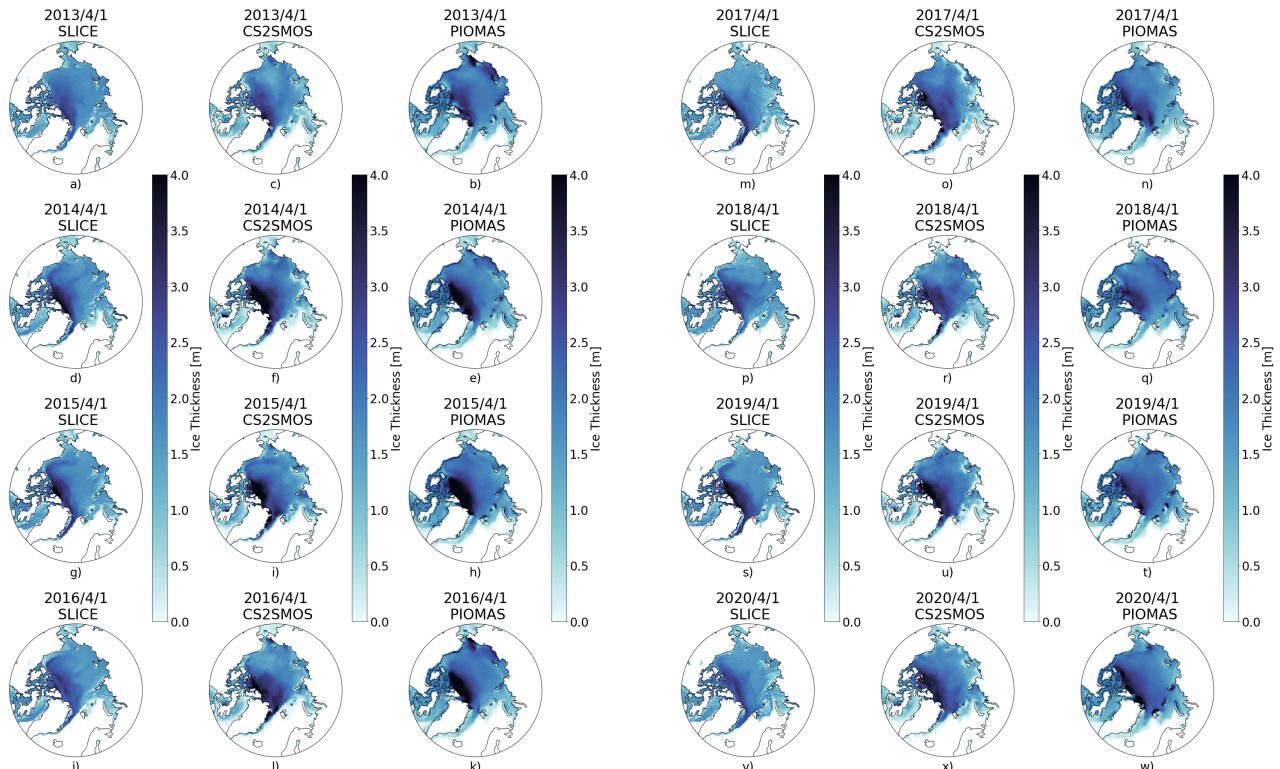


Figure A1. For the sea ice growth seasons ending in a–c) 2013, d–f) 2014, g–i) 2015, j–l) 2016, m–o) 2017, p–r) 2018, s–u) 2019 and v–x) 2020, a, d, g, j, m, p, v) SLICE sea ice thickness for 1 April, c, f, i, l, o, r, u, x) AWI CS2SMOS sea ice thickness from 1 April and b, e, h, k, n, q, t, w) PIOMAS sea ice thickness from 1 April.

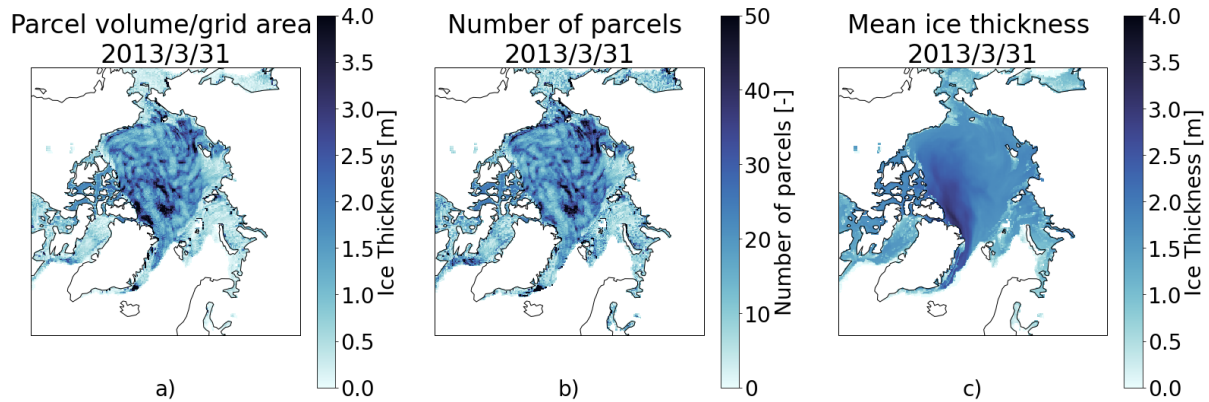


Figure A2. SLICE parcels on March 31 2013 (a) regridded using total parcel volume per grid cell divided by grid area, (b) counts within grid cell and (c) regridded mean parcel thickness within each grid cell. The volume per grid cell approach is unrealistic and dominated by erroneous convergence and divergence of parcels within grid cells.

760 *Author contributions.* All authors together conceived of the idea to use satellite retrieved snow–ice interface in a sea ice thickness satellite retrieval method. JA completed all analysis and wrote the first draft under guidance from YL and JK.

Competing interests. The authors declare that they have no conflict of interest.

765 *Acknowledgements.* This work was funded by the National Oceanic and Atmospheric Administration (NOAA) under grant no. NA20NES4320003. The views, opinions, and findings contained in this report are those of the author(s) and should not be construed as an official National Oceanic and Atmospheric Administration or U.S. Government position, policy, or decision. The merging of CryoSat-2 and SMOS data was funded by the ESA project SMOS & CryoSat-2 Sea Ice Data Product Processing and Dissemination Service and data from November 1st, 2012 to April 15th, 2021 were obtained from <https://www.meereisportal.de> (grant: REKLIM-2013-04).

References

Alexandrov, V., Sandven, S., Wahlin, J., , and Johannessen, O. M.: The relation between sea ice thickness and freeboard in the Arctic,
770 *Cryosphere*, 4, 373–380, <https://doi.org/10.5194/tc-4-373-2010>, 2010.

Bailey, E., Feltham, D. L., and Sammonds, P. R.: A model for the consolidation of rafted sea ice, *J. Geophys. Res.-Oceans*, 115, C04 015,
775 <https://doi.org/10.1029/2008jc005103>, 2010.

Batrak, Y., Kourzeneva, E., and Homleid, M.: Implementation of a simple thermodynamic sea ice scheme, SICE version 1.0-38h1,
780 within the ALADIN-HIRLAM numerical weather prediction system version 38h1, *Geoscientific Model Development*, 11, 3347–3368,
775 <https://doi.org/10.5194/gmd-11-3347-2018>, 2018.

Bitz, C. M. and Roe, G. H.: A mechanism for the high rate of sea ice thinning in the Arctic Ocean, *J. Climate*, 17, 3623–3632,
785 [https://doi.org/10.1175/1520-0442\(2004\)017<3623:amfthr>2.0.co;2](https://doi.org/10.1175/1520-0442(2004)017<3623:amfthr>2.0.co;2), 2004.

Cavalieri, D. J., Gloersen, P., and Campbell, W. J.: Determination of sea ice parameters with the Nimbus-7 SMMR, *J. Geophys. Res.-Atmos.*,
790 89, 5355–5369, <https://doi.org/10.1029/JD089iD04p05355>, 1984.

780 Cavalieri, D. J., Markus, T., and Comiso, J. C.: AMSR-E/Aqua Daily L3 25 km Brightness Temperature & Sea Ice Concentration Polar
785 Grids, Version 3, Boulder, Colorado USA. NASA National Snow and Ice Data Center Distributed Active Archive Center [data set],
780 https://doi.org/10.5067/AMSR-E/AE_SI25.003, 2014.

Comiso, J. C.: Sea ice effective microwave emissivities from satellite passive microwave and infrared observations, *J. Geophys. Res.-Oceans*,
790 88, 7686–7704, <https://doi.org/10.1029/JC088iC12p07686>, 1983.

785 Comiso, J. C.: Enhanced Sea Ice Concentrations and Ice Extents from AMSR-E Data, *Journal of The Remote Sensing Society of Japan*, 29,
780 199–215, <https://doi.org/10.11440/rssj.29.199>, 2009.

Connor, L. N., Laxon, S. W., Ridout, A. L., Krabill, W. B., and McAdoo, D. C.: Comparison of Envisat radar and airborne laser altimeter
795 measurements over Arctic sea ice, *Remote Sens. Environ.*, 113, 563–570, <https://doi.org/10.1016/j.rse.2008.10.015>, 2009.

Cox, G. F. N. and Weeks, W. F.: Numerical simulations of the profile properties of undeformed 1st-year sea ice during the growth season,
790 *Journal of Geophysical Research-Oceans*, 93, 12 449–12 460, <https://doi.org/10.1029/JC093iC10p12449>, 1988.

DeRepentigny, P., Tremblay, L. B., Newton, R., and Pfirman, S.: Patterns of Sea Ice Retreat in the Transition to a Seasonally Ice-Free Arctic,
795 *J. Climate*, 29, 6993 – 7008, <https://doi.org/10.1175/JCLI-D-15-0733.1>, 2016.

Docquier, D. and Koenigk, T.: Observation-based selection of climate models projects Arctic ice-free summers around 2035, *Nature Communications Earth & Environment*, 2, 144, <https://doi.org/10.1038/s43247-021-00214-7>, 2021.

790 Feltham, D. L., Untersteiner, N., Wettlaufer, J. S., and Worster, M. G.: Sea ice is a mushy layer, *Geophysical Research Letters*, 33, L14 501,
795 <https://doi.org/10.1029/2006gl026290>, 2006.

Gloersen, P. and Cavalieri, D. J.: Reduction of weather effects in the calculation of sea ice concentration from microwave radiances, *J. Geophys. Res.-Oceans*, 91, 3913–3919, <https://doi.org/10.1029/JC091iC03p03913>, 1986.

Guerreiro, K., Fleury, S., Zakharova, E., Kouraev, A., Remy, F., and Maisongrande, P.: Comparison of CryoSat-2 and ENVISAT radar
800 freeboard over Arctic sea ice: toward an improved Envisat freeboard retrieval, *Cryosphere*, 11, 2059–2073, <https://doi.org/10.5194/tc-11-2059-2017>, 2017.

Hall, D. K., Key, J. R., Casey, K. A., Riggs, G. A., and Cavalieri, D. J.: Sea ice surface temperature product from MODIS, *IEEE T. Geosci. Remote.*, 42, 1076–1087, <https://doi.org/10.1109/tgrs.2004.825587>, 2004.

Hendricks, S. and Ricker, R.: Product User Guide & Algorithm Specification: AWI CryoSat-2 Sea Ice Thickness (version 2.3),
 805 https://doi.org/10013/epic.ecd56b5d-3e7d-4a65-9019-588b1c3b0d26, 2020.

Hendricks, S., Paul, S., and Rinne, E.: ESA Sea Ice Climate Change Initiative (Sea_Ice_cci): Northern hemisphere sea
 ice thickness from the CryoSat-2 satellite on a monthly grid (L3C), v2.0. Centre for Environmental Data Analysis,
 https://doi.org/10.5285/ff79d140824f42dd92b204b4f1e9e7c2, 2018.

Hersbach, H., Bell, B., Berrisford, P., Biavati, G., Horányi, A., Muñoz Sabater, J., Nicolas, J., Peubey, C., Radu, R. and Rozum, I., Schepers,
 810 D., Simmons, A., Soci, C., Dee, D., and Thépaut, J.-N.: ERA5 hourly data on pressure levels from 1979 to present, Copernicus Climate
 Change Service (C3S) Climate Data Store (CDS) [data set], https://doi.org/10.24381/cds.bd0915c6, 2018.

Hersbach, H., Bell, B., Berrisford, P., Hirahara, S., Horanyi, A., Munoz-Sabater, J., Nicolas, J., Peubey, C., Radu, R., Schepers, D., Sim-
 mons, A., Soci, C., Abdalla, S., Abellán, X., Balsamo, G., Bechtold, P., Biavati, G., Bidlot, J., Bonavita, M., De Chiara, G., Dahlgren,
 815 P., Dee, D., Diamantakis, M., Dragani, R., Flemming, J., Forbes, R., Fuentes, M., Geer, A., Haimberger, L., Healy, S., Hogan, R. J.,
 Holm, E., Janiskova, M., Keeley, S., Laloyaux, P., Lopez, P., Lupu, C., Radnoti, G., de Rosnay, P., Rozum, I., Vamborg, F., Vil-
 laume, S., and Thepaut, J. N.: The ERA5 global reanalysis, Quarterly Journal of the Royal Meteorological Society, 146, 1999–2049,
 https://doi.org/10.1002/qj.3803, 2020.

Hewison, T. J. and English, S. J.: Airborne retrievals of snow and ice surface emissivity at millimeter wavelengths, IEEE T. Geosci. Remote.,
 37, 1871–1879, https://doi.org/10.1109/36.774700, 1999.

820 Hibler, W. D.: Dynamic Thermodynamic Sea Ice Model, J. Phys. Oceanogr., 9, 815–846, https://doi.org/10.1175/1520-
 0485(1979)009<0815:adtsim>2.0.co;2, 1979.

Hunke, E. and Lipscomb, H.: CICE: the Los Alamos Sea Ice Model Documentation and Software User's Manual, Version 4.1, LA-CC-
 06-012, https://doi.org/https://csdms.colorado.edu/w/images/CICE_documentation_and_software_user%27s_manual.pdf (last access: 27
 August 2021), 2010.

825 Kang, E. J., Sohn, B. J., Tonboe, R. T., Dybkjaer, G., Holmlund, K., Kim, J. M., and Liu, C.: Implementation of a 1-D Thermodynamic
 Model for Simulating the Winter-Time Evolvement of Physical Properties of Snow and Ice Over the Arctic Ocean, J. Adv. Model. Earth
 Sy., 13, 3, https://doi.org/10.1029/2020ms002448, 2021.

Key, J., Wang, X. J., Liu, Y. H., Dworak, R., and Letterly, A.: The AVHRR Polar Pathfinder Climate Data Records, Remote Sensing, 8, 3,
 https://doi.org/10.3390/rs8030167, 2016.

830 Kilic, L., Tonboe, R. T., Prigent, C., and Heygster, G.: Estimating the snow depth, the snow–ice interface temperature, and the effective
 temperature of Arctic sea ice using Advanced Microwave Scanning Radiometer 2 and ice mass balance buoy data, Cryosphere, 13, 1283–
 1296, https://doi.org/10.5194/tc-13-1283-2019, 2019.

Krabill, W. B., Thomas, R. H., Martin, C. F., Swift, R. N., and Frederick, E. B.: Accuracy of airborne laser altimetry over the Greenland
 ice-sheet, International Journal of Remote Sensing, 16, 1211–1222, https://doi.org/10.1080/01431169508954472, 1995.

835 Kurtz, N., Studinger, M., Harbeck, J., Onana, V., and Yi, D.: IceBridge L4 Sea Ice Freeboard, Snow Depth, and Thickness,
 Version 1., Boulder, Colorado USA. NASA National Snow and Ice Data Center Distributed Active Archive Center [data set],
 https://doi.org/10.5067/G519SHCKWQV6, 2015.

Kurtz, N. T., Farrell, S. L., Studinger, M., Galin, N., Harbeck, J. P., Lindsay, R., Onana, V. D., Panzer, B., and Sonntag, J. G.: Sea ice thickness,
 freeboard, and snow depth products from Operation IceBridge airborne data, Cryosphere, 7, 1035–1056, https://doi.org/10.5194/tc-7-
 840 1035-2013, 2013.

Kurtz, N. T., Galin, N., and Studinger, M.: An improved CryoSat-2 sea ice freeboard retrieval algorithm through the use of waveform fitting, *Cryosphere*, 8, 1217–1237, <https://doi.org/10.5194/tc-8-1217-2014>, 2014a.

Kurtz, N. T., Galin, N., and Studinger, M.: An improved CryoSat-2 sea ice freeboard retrieval algorithm through the use of waveform fitting, *Cryosphere*, 8, 1217–1237, <https://doi.org/10.5194/tc-8-1217-2014>, 2014b.

845 Kwok, R. and Cunningham, G. F.: ICESat over Arctic sea ice: Estimation of snow depth and ice thickness, *J. Geophys. Res.-Oceans*, 113, C08010, <https://doi.org/10.1029/2008jc004753>, 2008.

Kwok, R. and Cunningham, G. F.: Variability of Arctic sea ice thickness and volume from CryoSat-2, *Philos. T. Roy. Soc. A*, 373, 2045, <https://doi.org/10.1098/rsta.2014.0157>, 2015.

Kwok, R. and Rothrock, D. A.: Decline in Arctic sea ice thickness from submarine and ICESat records: 1958–2008, *Geophys. Res. Lett.*, 36, 850 <https://doi.org/10.1029/2009GL039035>, 2009.

Lavergne, T., Eastwood, S., Teffah, Z., Schyberg, H., and Breivik, L. A.: Sea ice motion from low-resolution satellite sensors: An alternative method and its validation in the Arctic, *J. Geophys. Res.-Oceans*, 115, C10 032, <https://doi.org/10.1029/2009jc005958>, 2010.

855 Lavergne, T., Sørensen, A. M., Kern, S., Tonboe, R., Notz, D., Aaboe, S., Bell, L., Dybkjaer, G., Eastwood, S., Gabarro, C., Heygster, G., Killie, M. A., Kreiner, M. B., Lavelle, J., Saldo, R., Sandven, S., and Pedersen, L. T.: Version 2 of the EUMETSAT OSI SAF and ESA CCI sea-ice concentration climate data records, *Cryosphere*, 13, 49–78, <https://doi.org/10.5194/tc-13-49-2019>, 2019.

Laxon, S. W., Giles, K. A., Ridout, A. L., Wingham, D. J., Willatt, R., Cullen, R., Kwok, R., Schweiger, A., Zhang, J. L., Haas, C., Hendricks, S., Krishfield, R., Kurtz, N., Farrell, S., and Davidson, M.: CryoSat-2 estimates of Arctic sea ice thickness and volume, *Geophys. Res. Lett.*, 40, 732–737, <https://doi.org/10.1002/grl.50193>, 2013.

860 Lee, S. M. and Sohn, B. J.: Retrieving the refractive index, emissivity, and surface temperature of polar sea ice from 6.9GHz microwave measurements: A theoretical development, *J. Geophys. Res.-Atmos.*, 120, 2293–2305, <https://doi.org/10.1002/2014jd022481>, 2015.

Lee, S. M., Sohn, B. J., and Kummerow, C. D.: Long-Term Arctic Snow/Ice Interface Temperature from Special Sensor for Microwave Imager Measurements, *Remote Sensing*, 10, 11, <https://doi.org/10.3390/rs10111795>, 2018.

Lei, R. B., Li, N., Heil, P., Cheng, B., Zhang, Z. H., and Sun, B.: Multiyear sea ice thermal regimes and oceanic heat flux derived from an ice mass balance buoy in the Arctic Ocean, *Journal of Geophysical Research-Oceans*, 119, 537–547, <https://doi.org/10.1002/2012jc008731>, 865 2014.

Leppäranta, M.: A Review of Analytical Models of Sea-Ice Growth, *Atmos. Ocean*, 31, 123–138, <https://doi.org/10.1080/07055900.1993.9649465>, 1993.

Lipscomb, W. H. and Hunke, E. C.: Modeling sea ice transport using incremental remapping, *Mon. Weather Rev.*, 132, 1341–1354, [https://doi.org/10.1175/1520-0493\(2004\)132<1341:msitui>2.0.co;2](https://doi.org/10.1175/1520-0493(2004)132<1341:msitui>2.0.co;2), 2004.

870 Liu, Y. H., Key, J. R., and Wang, X. J.: Influence of changes in sea ice concentration and cloud cover on recent Arctic surface temperature trends, *Geophys. Res. Lett.*, 36, L20 710, <https://doi.org/10.1029/2009gl040708>, 2009.

Liu, Y. H., Key, J., and Mahoney, R.: Sea and Freshwater Ice Concentration from VIIRS on Suomi NPP and the Future JPSS Satellites, *Remote Sensing*, 8, 6, <https://doi.org/10.3390/rs8060523>, 2016.

Liu, Y. H., Key, J. R., Wang, X. J., and Tschudi, M.: Multidecadal Arctic sea ice thickness and volume derived from ice age, *Cryosphere*, 14, 875 1325–1345, <https://doi.org/10.5194/tc-14-1325-2020>, 2020.

Markus, T. and Cavalieri, D. J.: An enhancement of the NASA Team sea ice algorithm, *IEEE T. Geosci. Remote.*, 38, 1387–1398, <https://doi.org/10.1109/36.843033>, 2000.

Markus, T. and Cavalieri, D. J.: The AMSR-E NT2 Sea Ice Concentration Algorithm : its Basis and Implementation, *Journal of The Remote Sensing Society of Japan*, 29, 216–225, <https://doi.org/10.11440/rssj.29.216>, 2009.

880 Markus, T., Neumann, T., Martino, A., Abdalati, W., Brunt, K., Csatho, B., Farrell, S., Fricker, H., Gardner, A., Harding, D., Jasinski, M., Kwok, R., Magruder, L., Lubin, D., Luthcke, S., Morison, J., Nelson, R., Neuenschwander, A., Palm, S., Popescu, S., Shum, C. K., Schutz, B. E., Smith, B., Yang, Y. K., and Zwally, J.: The Ice, Cloud, and land Elevation Satellite-2 (ICESat-2): Science requirements, concept, and implementation, *Remote Sens. Environ.*, 190, 260–273, <https://doi.org/10.1016/j.rse.2016.12.029>, 2017.

Markus, T., Comiso, J. C., and Meier, W. N.: AMSR-E/AMSR2 Unified L3 Daily 25 km Brightness Temperatures & Sea Ice Concentration 885 Polar Grids, Version 1, Boulder, Colorado USA. NASA National Snow and Ice Data Center Distributed Active Archive Center [data set], <https://doi.org/10.5067/TRUIAL3WPAUP>, 2018.

Massonnet, F., Vancoppenolle, M., Goosse, H., Docquier, D., Fichefet, T., and Blanchard-Wrigglesworth, E.: Arctic sea–ice change tied to its mean state through thermodynamic processes, *Nat. Clim. Change*, 8, 599–603, <https://doi.org/10.1038/s41558-018-0204-z>, 2018.

Mathew, N., Heygster, G., and Melsheimer, C.: Surface Emissivity of the Arctic Sea Ice at AMSR-E Frequencies, *IEEE T. Geosci. Remote.*, 890 47, 4115–4124, <https://doi.org/10.1109/tgrs.2009.2023667>, 2009.

Mayer, M., Tietsche, S., Haimberger, L., Tsubouchi, T., Mayer, J., and Zuo, H.: An Improved Estimate of the Coupled Arctic Energy Budget, *J. Climate*, 32, 7915–7934, <https://doi.org/10.1175/jcli-d-19-0233.1>, 2019.

Maykut, G. A. and Untersteiner, N.: Some results from a time-dependent thermodynamic model of sea ice, *Journal of Geophysical Research*, 76, 1550–+, <https://doi.org/10.1029/JC076i006p01550>, 1971.

895 McPhee, M. G. and Untersteiner, N.: Using sea ice to measure vertical heat-flux in the ocean, *Journal of Geophysical Research-Oceans*, 87, 2071–2074, <https://doi.org/10.1029/JC087iC03p02071>, 1982.

Mecklenburg, S., Drusch, M., Kerr, Y. H., Font, J., Martin-Neira, M., Delwart, S., Buenadicha, G., Reul, N., Daganzo-Eusebio, E., Oliva, R., and Crapolicchio, R.: ESA's Soil Moisture and Ocean Salinity Mission: Mission Performance and Operations, *IEEE T. Geosci. Remote.*, 50, 1354–1366, <https://doi.org/10.1109/tgrs.2012.2187666>, 2012.

900 Meier, W. N., Stewart, J. S., Liu, Y. H., Key, J., and Miller, J. A.: Operational Implementation of Sea Ice Concentration Estimates From the AMSR2 Sensor, *IEEE J. Sel. Top. Appl.*, 10, 3904–3911, <https://doi.org/10.1109/jstars.2017.2693120>, 2017.

Notz, D.: Thermodynamic and fluid-dynamical processes in sea ice, Ph.D. thesis, Cambridge University, 2005.

Panzer, B., Gomez-Garcia, D., Leuschen, C., Paden, J., Rodriguez-Morales, F., Patel, A., Markus, T., Holt, B., and Gogineni, P.: An ultra-wideband, microwave radar for measuring snow thickness on sea ice and mapping near-surface internal layers in polar firn, *Journal of 905 Glaciology*, 59, 244–254, <https://doi.org/10.3189/2013JoG12J128>, 2013.

Perovich, D., Richter-Menge, J., and Polashenski, C.: Observing and understanding climate change: Monitoring the mass balance, motion, and thickness of Arctic sea ice, <http://imb-crrl-dartmouth.org>, 2021.

Perovich, D. K. and Elder, B.: Estimates of ocean heat flux at SHEBA, *Geophysical Research Letters*, 29, <https://doi.org/10.1029/2001gl014171>, 2002.

910 Petty, A. A., Kurtz, N. T., Kwok, R., Markus, T., and Neumann, T. A.: Winter Arctic sea ice thickness from ICESat-2 freeboards, *Journal of Geophysical Research-Oceans*, 125, <https://doi.org/10.1029/2019JC015764>, 2020.

Polashenski, C., Perovich, D., Richter-Menge, J., and Elder, B.: Seasonal ice mass-balance buoys: adapting tools to the changing Arctic, *Ann. Glaciol.*, 52, 18–26, <https://doi.org/10.3189/172756411795931516>, 2011.

915 Richter-Menge, J. A., Perovich, D. K., Elder, B. C., Claffey, K., Rigor, I., and Ortmeyer, M.: Ice mass–balance buoys: a tool for measuring and attributing changes in the thickness of the Arctic sea–ice cover, *Ann. Glaciol.*, 44, 205–210, <https://doi.org/10.3189/172756406781811727>, 2006.

Ricker, R., Hendricks, S., Helm, V., Skourup, H., and Davidson, M.: Sensitivity of CryoSat-2 Arctic sea–ice freeboard and thickness on radar-waveform interpretation, *Cryosphere*, 8, 1607–1622, <https://doi.org/10.5194/tc-8-1607-2014>, 2014.

Ricker, R., Hendricks, S., Kaleschke, L., and Tian-Kunze, X.: CS2SMOS User Guide v3.0, <https://doi.org/10013/epic.51136>, 2017a.

920 Ricker, R., Hendricks, S., Kaleschke, L., Tian-Kunze, X., King, J., and Haas, C.: A weekly Arctic sea-ice thickness data record from merged CryoSat-2 and SMOS satellite data, *Cryosphere*, 11, 1607–1623, <https://doi.org/10.5194/tc-11-1607-2017>, 2017b.

Sallila, H., Farrell, S. L., McCurry, J., and Rinne, E.: Assessment of contemporary satellite sea ice thickness products for Arctic sea ice, *Cryosphere*, 13, 1187–1213, <https://doi.org/10.5194/tc-13-1187-2019>, 2019.

Saunders, R., Hocking, J., Turner, E., Rayer, P., Rundle, D., Brunel, P., Vidot, J., Roquet, P., Matricardi, M., Geer, A., Bormann, N., and Lupu, 925 C.: An update on the RTTOV fast radiative transfer model (currently at version 12), *Geoscientific Model Development*, 11, 2717–2732, <https://doi.org/10.5194/gmd-11-2717-2018>, 2018.

Schweiger, A., Lindsay, R., Zhang, J. L., Steele, M., Stern, H., and Kwok, R.: Uncertainty in modeled Arctic sea ice volume, *J. Geophys. Res.-Oceans*, 116, C00D06, <https://doi.org/10.1029/2011jc007084>, 2011.

Schwerdtfeger, P.: The Thermal Properties of Sea Ice, *Journal of Glaciology*, 4, 789–807, <https://doi.org/10.3189/S0022143000028379>, 1963.

930 Screen, J. A. and Simmonds, I.: The central role of diminishing sea ice in recent Arctic temperature amplification, *Nature*, 464, 1334–1337, <https://doi.org/10.1038/nature09051>, 2010.

Smolarkiewicz, P. K.: A fully multidimensional positive definite advection transport algorithm with small implicit diffusion, *J. Comput. Phys.*, 54, 325–362, [https://doi.org/10.1016/0021-9991\(84\)90121-9](https://doi.org/10.1016/0021-9991(84)90121-9), 1984.

Sohn, B. J. and Lee, S. M.: Analytical relationship between polarized reflectivities on the specular surface, *Int. J. Remote Sens.*, 34, 2368–935 2374, <https://doi.org/10.1080/01431161.2012.744490>, 2013.

Stefan, J.: Ueber die Theorie der Eisbildung, insbesondere über die Eisbildung im Polarmeere, *Ann. der Phy.-Berlin*, 278, 269–286, <https://doi.org/https://doi.org/10.1002/andp.18912780206>, 1891.

940 Stroeve, J. C., Serreze, M. C., Holland, M. M., Kay, J. E., Malanik, J., and Barrett, A. P.: The Arctic’s rapidly shrinking sea ice cover: a research synthesis, *Climatic Change*, 110, 1005–1027, <https://doi.org/10.1007/s10584-011-0101-1>, 2012.

Thorndike, A. S., Rothrock, D. A., Maykut, G. A., and Colony, R.: Thickness Distribution of Sea Ice, *J. Geophys. Res.-Oc. Atm.*, 80, 4501–4513, <https://doi.org/10.1029/JC080i033p04501>, 1975.

Tian-Kunze, X., Kaleschke, L., Maass, N., Makynen, M., Serra, N., Drusch, M., and Krumpen, T.: SMOS-derived thin sea ice thickness: algorithm baseline, product specifications and initial verification, *Cryosphere*, 8, 997–1018, <https://doi.org/10.5194/tc-8-997-2014>, 2014.

Tilling, R. L., Ridout, A., and Shepherd, A.: Estimating Arctic sea ice thickness and volume using CryoSat-2 radar altimeter data, *Adv. Space 945 Res.*, 62, 1203–1225, <https://doi.org/10.1016/j.asr.2017.10.051>, 2018.

Tschudi, M., Meier, W. N., Stewart, J. S., Fowler, C., and Maslanik, J.: Polar Pathfinder Daily 25 km EASE-Grid Sea Ice Motion Vectors, Version 4, Boulder, Colorado USA. NASA National Snow and Ice Data Center Distributed Active Archive Center [data set], <https://doi.org/10.5067/INAWUWO7QH7B>, 2019.

Tschudi, M. A., Meier, W. N., and Stewart, J. S.: An enhancement to sea ice motion and age products at the National Snow and Ice Data 950 Center (NSIDC), *Cryosphere*, 14, 1519–1536, <https://doi.org/10.5194/tc-14-1519-2020>, 2020.

Wang, X. J., Key, J., Kwok, R., and Zhang, J. L.: Comparison of Arctic Sea Ice Thickness from Satellites, Aircraft, and PIOMAS Data, *Remote Sensing*, 8, 9, <https://doi.org/10.3390/rs8090713>, 2016.

Wingham, D. J., Francis, C. R., Baker, S., Bouzinac, C., Brockley, D., Cullen, R., de Chateau-Thierry, P., Laxon, S. W., Mallow, U., Mavrocordatos, C., Phalippou, L., Ratier, G., Rey, L., Rostan, F., Viau, P., and Wallis, D. W.: CryoSat: A mission to determine the fluctuations in Earth's land and marine ice fields, *Natural Hazards and Oceanographic Processes from Satellite Data*, 37, 841–871, <https://doi.org/10.1016/j.asr.2005.07.027>, 2006.

955 Zhang, J. L. and Rothrock, D. A.: Modeling global sea ice with a thickness and enthalpy distribution model in generalized curvilinear coordinates, *Mon. Weather Rev.*, 131, 845–861, [https://doi.org/10.1175/1520-0493\(2003\)131<0845:mgsiwa>2.0.co;2](https://doi.org/10.1175/1520-0493(2003)131<0845:mgsiwa>2.0.co;2), 2003.